Coral anthozoan-specific opsins employ a novel chloride counterion for spectral tuning

Yusuke Sakai[1], Saumik Sen[2,3], Tomohiro Sugihara[1], Yukiya Kakeyama[1], Makoto Iwasaki[1], Gebhard F.X. Schertler[4], Xavier Deupi[2,3,4], Mitsumasa Koyanagi[1,5], Akihisa Terakita[1,5,*]

1. Department of Biology, Graduate School of Science, Osaka Metropolitan University, Sumiyoshi-ku, Osaka 558-8585, Japan.
2. Condensed Matter Theory Group, Laboratory for Theoretical and Computational Physics, Division of Scientific Computing, Theory, and Data, Paul Scherrer Institute, 5232 Villigen PSI, Switzerland.
3. Swiss Institute of Bioinformatics (SIB), Lausanne, Switzerland.
4. Laboratory of Biomolecular Research, Division of Biology and Chemistry, Paul Scherrer Institute, 5232 Villigen PSI, Switzerland.
5. The OMU Advanced Research Institute for Natural Science and Technology, Osaka Metropolitan University, Sumiyoshi-ku, Osaka 558-8585, Japan.

*Corresponding author:
Akihisa Terakita
Email: terakita@omu.ac.jp

Abstract

Animal opsins are G protein coupled receptors that have evolved to sense light by covalently binding a retinal chromophore via a protonated (positively charged) Schiff base. A negatively charged amino acid in the opsin, acting as a counterion, stabilises the proton on the Schiff base, which is essential for sensitivity to visible light. In this study, we investigate the spectroscopic properties of a unique class of opsins from a reef-building coral belonging to the anthozoan-specific opsin II group (ASO-II opsins), which intriguingly lack a counterion residue at any of established sites. Our findings reveal that, unlike other known animal opsins, the protonated state of the Schiff base in visible light-sensitive ASO-II opsins is highly dependent on exogenously supplied chloride ions (Cl^-). By using structural modelling and QM/MM calculations to interpret spectroscopy data, we conclude that, in the dark state, ASO-II opsins employ environmental Cl^- as their native counterion, while a nearby polar residue, Glu292 in its protonated neutral form, facilitates Cl^- binding. In contrast, Glu292 plays a crucial role in maintaining the protonation state of the Schiff base in the light-activated protein, serving as the counterion in the photoproduct. Furthermore, Glu292 is involved in G protein activation of the ASO-II opsin, suggesting that this novel counterion system coordinates multiple functional properties.

Introduction

Animals sense light by using opsins, photosensitive proteins belonging to the large family of G protein-coupled receptors (GPCRs). Opsins have a seven-transmembrane helix structure and bind to a retinal chromophore to form a light-sensitive pigment. Based on their phylogenetic relationships (Koyanagi and Terakita, 2014), eumetazoan animal opsins can be classified into eight groups with distinctive properties: vertebrate visual/non-visual opsins, opn3/TMT opsins, invertebrate Go-coupled opsins, cnidarian Gs-coupled opsins (cnidopsins), neuropsins (opn5), Gq-coupled visual pigments/melanopsins (opn4), peropsins, and retinochrome/RGR. Such diversity possibly underlies the diversification of light-dependent physiologies in animals. But, furthermore, this diversity also provides a range of potential optogenetic tools to manipulate intracellular G protein-mediated signaling (Koyanagi and Terakita, 2014).

Reef-building corals and sea anemones belong to the subphylum Anthozoa, which together with the subphylum Medusozoa constitute the phylum Cnidaria. Cnidarian animals possess multiple opsins categorised as part of the cnidarian Gs-coupled opsin group (cnidopsins), which regulate light-dependent processes (Koyanagi et al., 2008). For example, a member of this group is expressed in the ciliary type visual cells of the box jellyfish lens eyes (Koyanagi et al., 2008; Kozmik et al., 2008). Beyond these Gs-coupled cnidopsins, anthozoan animals have opsins phylogenetically distant from the other known eight groups, as well as opsins found exclusively in anthozoans (Feuda et al., 2012; Suga et al., 2008). These anthozoan-specific opsins (ASO) can be further classified into two groups, ASO-I and ASO-II (Gornik et al., 2020; Hering and Mayer, 2014; Mason et al., 2023; Picciani et al., 2018; Ramirez et al., 2016). Gornik et al. (2021) proposed that both ASO-I and ASO-II were present in the last common ancestor of Anthozoa and Medusozoa, but were lost secondarily in the Medusozoa lineage (Gornik et al., 2020). While it has been reported that both ASO-I and ASO-II are expressed in multiple tissues of sea anemones (Gornik et al., 2020; Suga et al., 2008) and corals (Levy et al., 2021), there is still a limited understanding of their molecular characteristics and physiological functions.

The members of the ASO-II group are not only phylogenetically unique but also display interesting features in their amino acid sequences. For instance, several of these opsins lack an amino acid residue conserved among typical opsins that is crucial for absorption of visible light (Gornik et al., 2020; Mason et al., 2023). While free retinal in solution has its absorption maximum (λ_{max}) in the ultraviolet (UV), this shifts to visible light when retinal is bound to a lysine residue in the transmembrane bundle of the opsin (usually at Lys296, numbering according to the bovine rhodopsin sequence) through a protonated Schiff base to form the pigment. Such protonated Schiff base is necessary to achieve sensitivity to visible light in opsin-based pigments (Pitt et al., 1955). However, the proton on the positively charged Schiff base is energetically unstable in the hydrophobic transmembrane environment. To stabilise this proton, a negatively charged residue, glutamic or aspartic acid, is situated near the Schiff base to act as a counterion. This counterion is essential for opsin-based pigments to absorb visible light, and the residues serving as the counterion are highly conserved across opsins (Terakita, 2005; Terakita et al., 2012). To date, three experimentally confirmed sites for the counterion have been identified in animal opsins: 94 in helix 2 (Gerrard et al., 2018), 113 in helix 3 (Nathans, 1990; Sakai et al., 2022; Sakmar et al., 1989; Zhukovsky and Oprian, 1989) and 181 in extracellular loop 2 (Nagata et al., 2019; Terakita et al., 2004, 2000). Remarkably, some opsins belonging to the ASO-II group lack glutamic or aspartic acid at any of these established counterion positions (Gornik et al., 2020; Mason et al., 2023). This absence raises the question of whether these opsins can absorb visible light, and if so, by what mechanism.

In this study, we investigate the spectroscopic properties of opsins in the ASO-II group isolated from the reef-building coral *Acropora tenuis*. Absorption spectra reveal that this group includes opsins sensitive to both UV and visible light. We then focus on a particular visible light-sensitive opsin within the ASO-II group (Antho2a) by spectroscopically analysing the protonated and deprotonated states of the Schiff base in the wild type and in single point mutants. By interpretating the spectroscopy data in the light of hybrid quantum mechanics/molecular mechanics (QM/MM) simulations, we demonstrate that a chloride anion (Cl^-) serves as a counterion to the retinylidene Schiff base in animal opsins, specifically in visible light-sensitive opsins of the ASO-II group.

86

87 # Results

88 **Identification of *Acropora tenuis* opsins**

89 We identified 17 opsins from the *Acropora tenuis* genome and transcriptome datasets by homology
90 search, which included eight opsins in Gs-coupled cnidopsin group, one opsin in the ASO-I group, and
91 eight opsins in the ASO-II group (Fig. S1; Fig. 1A). Full-length cDNAs of seven out of the eight
92 opsins in the ASO-II group were isolated and cloned from adult or larval tissues of the coral
93 (highlighted by bold letters in Fig. 1A). We failed to amplify one opsin in the ASO-II group (gene
94 model ID: aten_s0263.g14) by RT-PCR possibly because of its little mRNA expression level. Amino
95 acid sequence alignment shows that all the seven *A. tenuis* opsins in the ASO-II group lack a glutamic
96 or aspartic acid at the established counterion positions 94, 113 or 181 (Fig. S2). These opsins also have
97 no E(D)RY motif at the cytoplasmic end of helix 3, which is conserved throughout most class A
98 GPCRs (Hofmann et al., 2009).

99

100 **Absorption spectra of *Acropora tenuis* opsins in the ASO-II group**

101 We expressed seven members of the ASO-II group in COS-1 cells and purified their recombinant
102 pigments in detergent-solubilised conditions. We successfully obtained the absorption spectra of three
103 (Antho2a, Antho2c and Antho2e) out of the seven members, which showed that Antho2a and Antho2c
104 are visible light-sensitive opsins having with λ_{max} at 503 nm and 450 nm, respectively, whereas
105 Antho2e is a UV-sensitive opsin with λ_{max} at ~360 nm (Fig. 1B). We have previously reported that one
106 opsin in the ASO-II group, acropsin 4 of the coral *Acropora millepora*, induces a light-dependent
107 elevation of intracellular Ca^{2+} levels (Mason et al., 2023). Here, we showed that Antho2a, Antho2c and
108 Antho2e evoked a similar light-dependent increase of Ca^{2+} levels in HEK293S cells (Fig. 1C).

109

110 **Search for the counterion in *Acropora tenuis* opsins of the ASO-II group**

111 Antho2a and Antho2c form visible light-sensitive pigments in the dark (Fig. 1B) despite the lack of a
112 negatively charged counterion at any of the established positions (Fig. S2). To investigate how the
113 protonated Schiff base is stabilised in these opsins, we studied in more detail Antho2a (λ_{max} = 503 nm),
114 as it could be expressed well in cultured cells and was stable in detergent-solubilised conditions (Fig.
115 1B).
116
117 *(a) Contribution of Glu292 to the absorbance spectra of the dark state and photoproduct of Antho2a*
118 First, we searched for potential counterions at positions different from known established amino acid
119 sites (91, 113, and 181) in the Antho2a sequence. Using the crystal structure of bovine rhodopsin
120 (PDB ID: 1U19) as a template, we identified glutamic or aspartic acids located within 5Å of the Schiff
121 base in Antho2a and other members in the ASO-II group. Notably, all *A. tenuis* opsins in this group
122 contain a conserved glutamic/aspartic acid at position 292 (Fig. S2), positioned just one helix turn
123 away from the retinal-binding residue Lys296. To determine whether Glu292 could function as the
124 counterion in Antho2a, we mutated Glu292 to alanine and measured the absorption spectra. The
125 absorption spectrum of the E292A mutant in the dark was nearly identical to that of wild type (Fig.
126 2A, B, curve 1), exhibiting a clear absorbance in the visible light region with only a slightly red-
127 shifted λ_{max} (505 nm) at 140 mM NaCl and pH 6.5. This shows that a negative charge other than
128 Glu292 may serve as a counterion in the dark state of wild type Antho2a.
129 We next investigated the spectroscopic properties of the photoproduct of wild type Antho2a and
130 the E292A mutant. Upon irradiation of wild type Antho2a with orange light, the λ_{max} shifted from 503
131 nm in the dark to 476 nm in the photoproduct (Fig. 2A, curve 2; Fig. S3A, curves 2 and 3). This shift
132 is due to the photoisomerisation of the 11-*cis* retinal chromophore to its all-*trans* form, converting
133 almost 100% of the dark state to the photoproduct (Fig. S3B). The photoproduct remained stable for at
134 least 5 minutes (Fig. S3A, curve 2 and curve 3), but it exhibited a gradual decay (Fig. S3C, D),
135 indicating that purified Antho2a is neither strictly bleach resistant nor bistable (see also Fig. S3
136 legend). In contrast to the dark state, the photoproduct of the E292A mutant displayed two distinct
137 absorption peaks in UV and visible light regions, at ~370 nm and 476 nm respectively (Fig. 2B, curve

138 2). This suggests that the E292A mutation causes UV-light absorption due to a deprotonated Schiff
139 base in the photoproduct. Additionally, altering the pH modified the ratio of absorbance between the
140 ~370 nm and 476 nm peaks in the E292A mutant (Fig. S4B, curves 2), with the UV-peak to the visible
141 light-peak ratio increasing at higher pH levels (pH 7.5, Fig. S4B, curve 2). Conversely, the wild type
142 did not exhibit an increase in UV absorbance under similar high pH condition (pH 7.5, Fig. S4A,
143 curve 2). These results indicate that the Schiff base in the photoproduct of the Antho2a E292A mutant
144 has a lower acid dissociation constant (pK_a) than that of the wild type, suggesting that Glu292 acts as
145 the counterion in the photoproduct of Antho2a.

146 We then further explored the nature of the counterion in the dark state of Antho2a. Previous
147 studies have shown that in the bovine rhodopsin E113A and E113Q mutants, as well as in the
148 retinochrome E181Q mutant (referred to as "counterion-less" mutants), halide ions like Cl^- can act as
149 "surrogate" counterions to stabilise the proton on the Schiff base. Consequently, these counterion-less
150 mutants can still absorb visible light in the presence of Cl^- (Nathans, 1990; Sakmar et al., 1991;
151 Terakita et al., 2000). To assess the potential role of Cl^- as a surrogate counterion in the dark state of
152 the Antho2a E292A mutant, we performed spectroscopic analyses under Cl^--depleted conditions (Fig.
153 2C, D). We observed that the λ_{max} of the E292A mutant shifted to the UV region (Fig. 2D, curve 1).
154 Unexpectedly, a similar shift in absorption to the UV region was also observed in the wild type under
155 the Cl^--depleted condition (Fig. 2C, curve 1). These results indicate that, in the absence of Cl^-, the
156 Schiff base in both the wild type and the E292A dark states becomes deprotonated. The subsequent
157 addition of Cl^- (final concentration: 140 mM NaCl) restored clear absorbance in the visible light
158 region (Fig. 2C, D, curves 2), showing that Cl^- facilitates the protonation of the Schiff base of the dark
159 state even in the wild type. In contrast, the photoproduct of the wild type exhibited no significant
160 change in the ratio of UV to visible-light absorption peaks at pH 6.5 across NaCl concentrations from
161 0.28 mM to 800 mM (Fig. S5). The wild type consistently absorbed visible light under these NaCl
162 conditions (curves 2 in Fig. S5A, B), suggesting that Cl^- has little impact on the Schiff base pK_a in the
163 photoproduct of wild type Antho2a. However, the photoproduct of the E292A mutant exhibited a pH-
164 dependent shift in the ratio of UV to visible-light absorption between pH 4.8 and pH 7.6, even at 800

165 mM NaCl, where the dark state predominantly absorbed visible light (Fig. S5C). This further supports
166 that Glu292 serves as the counterion in the photoproduct of Antho2a.
167
168 *(b) Effect of halide anions on λ_{max} values of the dark state of Antho2a*
169 To obtain a further evidence supporting the Cl^- counterion in the dark state of Antho2a, we examined
170 the impact of different halide anions on the absorption spectrum in the dark state of Antho2a, as
171 observed in the bovine rhodopsin counterion-less mutant (Nathans, 1990; Sakmar et al., 1991).
172 Antho2a readily absorbed visible light in the presence of bromide ion (Br^-) and iodide ion (I^-) as well
173 as Cl^- and the λ_{max} of wild type Antho2a shifted depending on the halide solutions (503 nm in 140 mM
174 NaCl; 506 nm in 140 mM NaBr; 511 nm in 140 mM NaI solutions; Fig. S6A). The E292A mutant
175 showed a similar shift in λ_{max} (505 nm in 140 mM NaCl; 507 nm in 140 mM NaBr; 517 nm in 140
176 mM NaI solutions; Fig. S6B).
177
178 *(c) Effect of Cl^- concentration on the pK_a of the protonated Schiff base of Antho2a*
179 To further investigate the influence of Cl^- on the protonation state of the Schiff base in the dark state
180 of Antho2a, we estimated the pK_a of the Schiff base by measuring the pH dependent-changes in the
181 absorption spectra of Antho2a at different Cl^- concentrations. The pH-dependent equilibrium between
182 the visible (protonated Schiff base) and UV (deprotonated Schiff base) forms revealed that their ratio
183 changes with Cl^- concentration (Fig. S7A–E). A plot of the changes in absorbance at λ_{max} against pH
184 (Fig. 3A) shows that in wild type Antho2a, the pK_a of the protonated Schiff base increases with higher
185 Cl^- concentrations (7.3 at 0.28 mM NaCl, 8.0 at 2.8 mM, 8.8 at 28 mM, 8.8 at 140 mM, and 9.0 at 500
186 mM). We failed to determine the pK_a at 0 mM NaCl, as the observed λ_{max} in acidic conditions (pH <
187 6.5) were shorter than expected in Antho2a (503 nm), suggesting that a normal pigment was not
188 produced under these conditions (Fig. S8A). Similarly, the Cl^- concentration also affected the pK_a of
189 the protonated Schiff base in the E292A mutant (6.1 at 2.8 mM NaCl, 6.8 at 28 mM, 7.7 at 140 mM,
190 and 8.9 at 500 mM) (Fig. 3B; Fig. S9). At 0 mM NaCl, the E292A mutant showed no visible light
191 absorption, even under the most acidic conditions (pH 4.7), preventing the determination of its pK_a

192 (Fig. S8B). Notably, at low Cl^- concentrations (2.8 mM NaCl), the wild type exhibited a higher pK_a
193 than the E292A mutant (8.0 and 6.1, respectively). However, at 500 mM NaCl, the pK_a of the E292A
194 mutant and wild type were comparable (9.0 and 8.9, respectively; Fig. 3A, B). These results suggest
195 that Cl^-, rather than Glu292, serves as the counterion in the dark state of Antho2a, while Glu292
196 facilitates the protonation of the Schiff base by the Cl^- counterion.
197
198 *(d) Binding affinity of Cl^- to wild type Antho2a and the E292A mutant*
199 To evaluate the Cl^- binding affinities of both wild type Antho2a and the E292A mutant, we measured
200 changes in their absorption spectra by gradually increasing Cl^- concentrations at pH 6.5 and estimated
201 the Cl^- dissociation coefficients (K_d). The relative absorbance in the visible region increased with
202 higher Cl^- concentrations both in the wild type and the E292A mutant (Fig. S10A, B). By fitting the
203 Hill equation to the experimental data (Fig. 3C), the dissociation constants (K_d) of Cl^- were
204 determined to be 0.079 ± 0.010 mM for the wild type Antho2a and 12.7 ± 0.519 mM for the E292A
205 mutant. This significant increase in the K_d value for the E292A mutant suggests that the Cl^- binding
206 affinity is considerably reduced due to the mutation. Consequently, we suggest that while Glu292 does
207 not act as a direct counterion, it plays a crucial role in facilitating Cl^- binding to Antho2a.
208
209 **Structural modelling and QM/MM calculations of the dark state of Antho2a**
210 To gain a deeper understanding of the environment surrounding the retinylidene Schiff base in the
211 dark state of Antho2a, we performed QM/MM-based structural modelling of both the wild type
212 Antho2a (with Glu292 either neutral or negatively charged) and the E292A mutant. The QM/MM
213 geometry optimisation positioned the Cl^- ion close to the Schiff base (~3Å) and near Glu292 (~4.7Å),
214 with Glu292 itself located in proximity to the Schiff base (~3.3Å) (Fig. 4A, B). To validate these
215 models, we calculated the QM/MM vertical excitation energies of the ground state geometries (Table
216 S1).
217 For wild type Antho2a with a protonated neutral Glu292, the calculated λ_{max} using the CAM-
218 B3LYP/cc-pVTZ level of theory was 503 nm (Fig. 4A), in good agreement with the experimentally

observed value (503 nm; Fig. 2A). In contrast, the λ_{max} calculated with a deprotonated negatively charged Glu292 was blue-shifted to 415 nm (Fig. 4B), deviating significantly from the experimental value. Finally, the calculated λ_{max} for the E292A mutant was 499 nm (Fig. 4C), also in agreement with the experimental value (505 nm). To further substantiate these findings, we recalculated the excitation energies using the RI-ADC(2)/cc-pVTZ method. Although these λ_{max} values are blue-shifted compared to those calculated with the CAM-B3LYP method, they followed a similar trend. Both these computational methods have previously been employed to accurately calculate the excitation energies of rhodopsins (Church et al., 2021). These results strongly suggest that in the dark state of Antho2a, Glu292 is protonated and neutral at pH 6.5, and therefore, it does not function as the counterion.

Effect of the Glu292 mutation on the function of the photoproduct

The spectroscopy data indicate that Glu292 is involved in stabilising the protonated Schiff base by facilitating Cl^--binding in the dark state and also serves as a counterion in the photoproduct. This suggests that Glu292 significantly contributes to the visible light absorption of Antho2a. To explore additional roles of Glu292 in Antho2a, we measured the light-induced Ca^{2+} response in cultured cells expressing wild type Antho2a or the E292A mutant. Notably, cells expressing wild type Antho2a showed a ~30-fold increase in Ca^{2+} levels upon light irradiation (Fig. 5, solid black circles), whereas cells expressing the Antho2a E292A mutant showed a smaller Ca^{2+} elevation (< 5-fold increase) (Fig. 5, red open circles). This indicates that the peak Ca^{2+} response in cells expressing wild type Antho2a was approximately nine times greater than in cells expressing the E292A mutant. This result, along with the crucial role of Glu292 in Cl^- binding in the dark state and as a counterion in the photoproduct, suggests that Glu292 plays also a role in G protein activation.

Cl^--dependent changes in the absorption spectra of the dark states of Antho2c and Antho2e

We tested whether Cl^- concentration affects the pK_a of the Schiff base in another visible light-sensitive opsin, Antho2c (λ_{max} = 450 nm, Fig. 1B). The pH-dependent equilibrium between UV- and visible-light absorbing forms was clearly observed at 0 mM or 0.093 mM NaCl, but not at 9.3 mM NaCl,

where Antho2c stably absorbed visible light across the measured pH range (pH 4.8 to 7.2, Fig. 6A–C). Also, the ratio of UV to visible-light absorption increased with higher Cl^- concentrations at pH 6.5 (Fig. 6D). These results demonstrate that Cl^- serves as a counterion in the dark state of Antho2c, as it does in Antho2a. In contrast, wild type Antho2e continues to absorb UV light even at 1 M NaCl (Fig. 6E). Notably, Antho2e has an arginine at position 113, which corresponds to the counterion position in vertebrate visual opsins (Fig. S2). When this arginine is mutated to alanine (R113A), the mutant becomes sensitive to visible light (λ_{max} = ~420 nm) in the presence of Cl^- (Fig. 6F), suggesting that Cl^- can serve as the counterion in the R113A mutant.

Discussion

In this study, we reveal for the first time the spectral properties of opsins in the ASO-II group from the coral *Acropora tenuis*, showing that their sensitivity spans from UV to visible light. Opsins in this group have a highly conserved Glu292 residue near the Schiff base, which can potentially stabilise the proton on the Schiff base. Indeed, our results show that the pK_a of the protonated Schiff base in the photoproduct (λ_{max} = 476 nm) of Antho2a is altered when Glu292 is substituted with alanine (Fig. 2A, B; Fig. S4), suggesting that Glu292 serves as the counterion of the photoproduct. Conversely, the dark state of Antho2a (λ_{max} = 503 nm) exhibits robust visible light absorption only in the presence of Cl^- at physiological pH, and the pK_a of the protonated Schiff base changes with Cl^- concentration in both wild type Antho2a and the E292A mutant. Furthermore, the pK_a for wild type and the E292A mutant are comparable in the presence of sufficient Cl^- (500 mM NaCl, Fig. 3A, B), supporting the conclusion that Cl^-, and not Glu292, acts as the counterion of the dark state of *A. tenuis* Antho2a. We found that the type of halide anions in the solution affected the λ_{max} values of the dark state of Antho2a, which is consistent with the observed effect on the λ_{max} of the bovine rhodopsin counterion-less mutant, in which halide ion serves as a surrogate counterion (Nathans, 1990; Sakmar et al., 1991), further substantiating our hypothesis that a solute anion acts as the counterion in the dark state of Antho2a. Moreover, QM/MM calculations for the dark state of Antho2a suggest that Glu292 is

protonated and neutral, further supporting the hypothesis that Glu292 does not serve as the counterion in the dark state. Along with the result showing Cl^- has little to no effect on the visible light absorption of the photoproduct (Fig. S5), unlike the wild type, we conclude that Cl^- and Glu292, respectively, act as counterions for the protonated Schiff base of the dark state and photoproduct of Antho2a. This represents a unique example of counterion switching from exogeneous anion to a specific amino acid residue upon light irradiation.

Our spectroscopic data also showed that the other visual light sensitive opsin, Antho2c, exhibited the Cl^- dependency on the Schiff base pK_a of the dark state, which suggesting that opsins in the ASO-II group may share a spectral tuning mechanism based on the Cl^- counterion. Interestingly, Antho2e had an arginine at position 113 and when it was mutated to alanine (R113A), the mutant showed sensitivity to visible light in the presence of Cl^- (Fig. 6F). We hypothesise that the positive charge of Arg113 disturbs interaction between the Cl^- and the protonated Schiff base or that it completely inhibits Cl^- binding, rendering Antho2e UV-sensitive.

It is noteworthy that although Cl^- has been reported to serve as a surrogate counterion in "counterion-less" mutants of animal opsins (such as E113Q in bovine rhodopsin and E181Q in retinochrome) (Nathans, 1990; Sakmar et al., 1991; Terakita et al., 2000), Antho2a is, to our knowledge, the first example in a wild type animal opsin that employs Cl^- as a counterion. Interestingly, within the microbial rhodopsin family, heliorhodopsin (TaHeR) incorporates a Cl^- into the Schiff base region under high Cl^- concentrations at pH 4.5. This Cl^- stabilises the protonated retinal Schiff base when its primary counterion, E108, is neutralised (Besaw et al., 2022). The observed 18 nm red shift at low pH is consistent with E108 protonation. The TaHeR E108A mutant shows the same λ_{max} under high Cl^- concentrations, further supporting the role of Cl^- as a counterion. At pH 8, the Schiff base proton is stabilised by the negatively charged E108 (Shihoya et al., 2019).

The E292A mutation in Antho2a drastically decreases the Cl^- binding affinity in the dark state at pH 6.5 (K_d: Antho2a WT = 0.079 mM, Antho2a E292A = 12.7 mM). Based on these results, supported by our QM/MM calculations of the dark state, we hypothesise that protonated Glu292 not only serves as a counterion of the photoproduct but also constitutes part of the Cl^- binding site in the dark state of

299 Antho2a. In Cl^--pumping microbial rhodopsins, where Cl^- serves as a counterion, the Cl^- binding site
300 near the Schiff base is typically formed by hydrogen-bonding between Cl^-, the protonated Schiff base,
301 and key amino acids such as serine, threonine and aspartic acid, and water molecules (Besaw et al.,
302 2020; Hosaka et al., 2016; Kolbe et al., 2000). Additionally, the bovine rhodopsin double mutant
303 E113Q/A292E exhibits a higher sensitivity to hydroxylamine than the wild type, indicating instability
304 of the Schiff base and increased solvent accessibility (Tsutsui and Shichida, 2010). These observations
305 suggest that Glu292 in Antho2a may also facilitate the accessibility of Cl^- ions to the Schiff base
306 environment. To determine the precise nature of the Cl^- binding site and clarify the roles of Glu292
307 and other residues in the Cl^--dependent counterion system of Antho2a, detailed spectroscopic and
308 structural experiments will be necessary.

309 We also found that the cells expressing the Antho2a E292A mutant show a lower Ca^{2+} elevation
310 upon light stimulation compared to the wild type (Fig. 5). This effect could be due to Glu292 not only
311 serving as a counterion in the photoproduct but also allosterically influencing G protein activation. It
312 has been reported that the introduction of Glu or Asp at position 292 can affect various molecular
313 properties of opsins. For instance, the A292E mutation in human rhodopsin has been shown to result
314 in constitutively active apoproteins, leading to congenital night blindness (Dryja et al., 1993; Jin et al.,
315 2003). These data suggest that Glu292 has the potential to influence functional properties, such as G
316 protein activation. Several studies have reported that the counterion can affect diverse properties of
317 opsins beyond their absorption spectra. For instance, in bovine rhodopsin, Glu113 is involved not only
318 in visible light absorption in the dark state but also in the efficient activation of G proteins by the
319 photoproduct (Terakita et al., 2004). It has been suggested that these pleiotropic functions of the
320 counterion have been achieved through evolutionary modifications of the protein structure once the
321 counterion was acquired (Terakita et al., 2004). This concept may similarly apply to Antho2a.

322 One of the notable features of the opsins in the ASO-II group that use chloride as a counterion is
323 the relatively low pK_a of the Schiff base (e.g., ~9.0 for Antho2a in the dark state, Fig. 3A) compared to
324 other animal opsins with a "regular" amino acid counterion (e.g., >16 for bovine rhodopsin, with
325 Glu113 as a counterion (Steinberg et al., 1993) or 11 for jumping spider Rh1, with Glu181 as a

326 counterion (Nagata et al., 2019)). We hypothesise that opsins in the ASO-II group, with lower Schiff
327 base pK_a, may change their spectral sensitivity and G protein activation profile within the
328 physiological pH range of corals. For instance, these opsins could exhibit decreased sensitivity to
329 visible and increased sensitivity to UV light under alkaline pH conditions. The extra- and intracellular
330 pH environments in symbiotic cnidarians such as corals are spatially and temporally variable due to
331 the photosynthesis of symbiotic algae (Barott et al., 2017). For example, pH values in the cytosol of
332 algae-hosting cells (a group of endodermal cells with algal occupancy) in corals reportedly increase by
333 approximately 0.5 pH units upon light treatment (Venn et al., 2009). The pH values in the
334 gastrovascular cavity (coelenteron), which is in contact with endodermal cells, range from 6.6 to 8.5
335 (Agostini et al., 2012; Al-Horani et al., 2003; Cai et al., 2016) and increase in the presence of light,
336 presumably due to the consumption of CO_2 by photosynthesis (Barott et al., 2017). Additionally,
337 alkalinisation in extracellular region of calcifying cells reportedly increases ~1.0 pH units from dark to
338 light conditions reaching levels above pH 9.0 (Al-Horani et al., 2003). These pH changes, generally an
339 increase due to photosynthetic activity, may result in variable light sensitivity of the "low pK_a" opsins
340 in the ASO-II group. Recent studies have reported that members of the ASO-II group may be
341 associated with the symbiotic relationship between host anthozoans and symbiotic algae. For example,
342 using the symbiotic sea anemone *Exaiptasia diaphana*, Gornik et al. (2021) showed that the mRNA
343 levels of several opsins in the ASO-II group were higher in symbiotic adults than in apo-symbiotic
344 ones (Gornik et al., 2020). In sea anemone, it has also been reported that behavioural responses to light
345 differ between symbiotic and apo-symbiotic individuals (Foo et al., 2020; Kishimoto et al., 2023),
346 with these responses potentially being driven by the activation of ASO-II opsins that are up-regulated
347 in the presence of symbiotic algae. Moreover, single-cell RNA-seq analysis in the reef-building coral
348 *Stylophora pistillata* has revealed that an opsin belonging to the ASO-II group is specifically
349 expressed in algae-hosting cells (a group of endodermal cells with 50% algal occupancy) (Levy et al.,
350 2021). Although further studies are needed, we suggest that the unique use of Cl^- as the counterion in
351 opsins of ASO-II group, rather than a negatively charged amino acid, may be associated to their pH-

352 sensitive light response and, ultimately, to their role in photosynthesis-related functions in symbiotic
353 cnidarians.
354 It is widely accepted that opsins have evolved from a non-opsin GPCR (Feuda et al., 2012). Our
355 finding of the native chloride counterion in opsins shows a possibility that in the first stage of the
356 evolutionary process, the "primitive" opsins having Lys296 but no counterion residue could absorb not
357 only UV light but also a wide range of wavelengths that extends into the visible region by embracing
358 chloride ions. Namely, the chloride counterion system might have been a preliminary step in the
359 evolution of amino acid counterions in animal opsins. Further empirical and bioinformatic studies are
360 required for disentangling the evolutionary trajectories of the Schiff base – counterion system,
361 including the chloride counterion.
362

363 # Materials and Methods

364 **Experimental design**

365 We first identified and cloned opsins from a reef-building coral, *Acropora tenuis*, and then expressed
366 opsins belong to the ASO-II group in mammalian cultured cells. We performed spectroscopic
367 measurements of purified pigments of the opsins in different pH and Cl^- conditions to identify their
368 effects on the acid dissociation constant of the protonated Schiff base of the opsins, leading to the
369 determination of the counterion. Computational modelling and QM/MM calculations were also
370 conducted to elucidate the retinylidene Schiff base environment in the dark state of Antho2a. Light-
371 evoked Ca^{2+} responses were assessed by aequorin-based bioluminescent reporter assay to evaluate the
372 G protein activation of Antho2a.
373

374 **Identification of *Acropora tenuis* opsins and phylogenetic tree inference**

375 *Acropora tenuis* (Dana, 1846) is a common reef-building coral distributed throughout the Indo-Pacific
376 Ocean. Candidate sequences of *A. tenuis* opsins were identified by homology search against public
377 genome and transcriptome datasets (Shinzato et al., 2020; Voolstra et al., 2015) and their phylogenetic

378 relationships to known opsins were inferred by subsequent phylogenetic tree reconstruction. We first
379 conducted BLASTP and TBLASTN searches with an E-value cut-off of 10^{-10} using *Acropora palmata*
380 Acropsin 1–3 (JQ966100 – JQ966102), two *Nematostella vectensis* opsins (BR000676 – BR000677),
381 human rhodopsin (NM_000539), and squid rhodopsin (X70498) as queries. We aligned the collected
382 opsin homologs and excluded sequences which did not contain a retinal-binding lysine residue
383 (Lys296) in the seventh transmembrane helix. We modified the fragmented sequences by reference to
384 the genome sequence of *A. tenuis* and opsin sequences of other *Acropora* species (*A. palmata* or *A.*
385 *millepora*). The candidate sequences of *A. tenuis* opsins were combined with the representative opsin
386 sequences. The final sequence set was aligned using MAFFT (Katoh and Standley, 2013) and trimmed
387 by TrimAl (Capella-Gutiérrez et al., 2009) with the "*gappyout*" function. The ML tree was
388 reconstructed using RAxML-NG v1.1.0 (Kozlov et al., 2019) assuming the LG + G4 model of protein
389 evolution, which was selected by ModelTest-NG v0.2.0 (Darriba et al., 2020). The ML branch
390 supports were estimated with 1000 bootstrap replicates.
391
392 **Sample collection, total RNA extraction, and cDNA synthesis**
393 Colonies of *A. tenuis* were collected from < 3 m depth on the fringing reef on Sesoko Island, Okinawa
394 (N26°37.58′, E127°52.01′) and were maintained in flow-through aquaria at Sesoko Station (Tropical
395 Biosphere Research Center, University of Ryukyus, Okinawa, Japan). Four days after spawning,
396 motile larvae and small branches of adult colonies were preserved in RNAlater® Stabilization
397 Solution (Thermo Fisher Scientific, MA, USA). Total RNAs were extracted from the larval and adult
398 samples using TRIzol reagent (Thermo Fisher Scientific) or Sepasol-RNA I Super G (nacalai tesque,
399 Kyoto, Japan) and purified using Qiagen RNeasy mini kits (Qiagen, Hilden, Germany) following the
400 manufacturer's protocol. cDNAs were synthesised from the total RNA by reverse transcription using
401 High-Capacity cDNA Reverse Transcription kits (Thermo Fisher Scientific).
402
403 **Expression and purification of *Acropora tenuis* opsins**

404 The coding regions of *A. tenuis* opsins were amplified by PCR with gene-specific primers and were
405 tagged with the epitope sequence of the anti-bovine rhodopsin antibody Rho1D4 (ETSQVAPA) at
406 their C-termini. Site-directed mutants were produced by overlap extension PCR using PrimeSTAR
407 Max DNA Polymerase (TAKARA, Shiga, Japan) with site-specific primers and were also tagged with
408 the 1D4 epitope sequence. The tagged cDNAs were inserted into the pUSRα vector (Kayada et al.,
409 1995) digested with HindIII and EcoRI or the pMT vector (Ridge and Abdulaev, 2000) digested with
410 EcoRI and NotI using In-Fusion HD cloning kit (TAKARA). The plasmids (15 μg per 100 mm culture
411 dish) were transfected into COS-1 cells using the polyethyleneimine (PEI) transfection method. The
412 transfected cells were maintained for 24 h after transfection at 37°C under 5% CO_2 and then 11-*cis*
413 retinal was added to the medium (1 μL of 4 mM 11-*cis* retinal to 100 mm culture dish) following 25°C
414 or 30°C incubation for another 24 h in the dark before collecting the cells. The reconstituted pigments
415 were extracted from the cell membranes with 1% dodecyl β-D-maltoside (DDM, Dojindo, Kumamoto,
416 Japan), 50 mM HEPES, and 140 mM NaCl (pH 6.5). The solubilised samples were mixed with 1D4-
417 condjugated agarose beads overnight, and the mixture was transferred into Bio-Spin columns (Bio-
418 Rad, Hercules, CA, USA) and washed in the buffer containing 0.02% DDM, 50 mM HEPES, and 140
419 mM NaCl (pH 6.5, buffer A). The purified pigments were eluted with buffer A containing 0.5 ~ 1
420 mg/mL 1D4 peptide (custom peptide synthesis by GenScript Japan Inc., Tokyo, Japan). To obtain
421 pigments in solutions of various anions (SO_4^{2-}, Br^-, and I^-) other than Cl^-, samples were prepared as
422 described above and in the final step the mixture of solubilised samples and 1D4-agarose beads was
423 washed with buffer A followed by the additional wash with buffers including different sodium salts of
424 anions (0.02% DDM, each of 70 mM Na_2SO_4, 140 mM NaBr, or 140 mM NaI, and 50 mM HEPES).
425 Then the pigments were eluted with the buffer including the appropriate sodium salt of anion
426 containing 0.5 ~ 1 mg/mL 1D4 peptide. Alternatively, for some pigments that were unstable under the
427 absence of Cl^-, we quickly removed Cl^- by gel-filtration chromatography on PD MiniTrap desalting
428 columns with Sephadex G-25 resin (Cytiva, Marlborough, MA, USA). The columns were first
429 equilibrated with the buffer including 0.02% DDM, 70 mM Na_2SO_4, and 50 mM HEPES, 500 μL of

430 samples were loaded onto the columns and eluted with the buffer. We collected 800 μL fractions and
431 used them for subsequent spectroscopic analyses.
432
433 **UV-visible spectroscopy**
434 Spectroscopic measurements were performed at 0°C using a V-750 UV-visible spectrophotometer
435 (JASCO Corporation, Tokyo, Japan). The pH of the samples was adjusted with 100 mM CAPS
436 including NaOH for alkaline conditions and 500 mM NaH_2PO_4 for acidic conditions. pH values were
437 measured using a pH meter (B-211; HORIBA, Kyoto, Japan) immediately after each spectroscopic
438 measurement. The concentration of Cl^- in the samples was adjusted by addition of different
439 concentrations of NaCl solutions which were prepared in 70 mM Na_2SO_4 buffer (see above). A 100-W
440 halogen lamp was equipped on the spectrophotometer and used to illuminate samples with a set of
441 optical interference filters (420 nm, Toshiba) and cut-off filters (O-55 or O-56, AGC Techno Glass
442 Co., Shizuoka, Japan). Absorption spectra of some UV-absorbing pigments were recorded using the V-
443 750 UV-visible spectrophotometer, equipped with a 300-W xenon lamp (MAX-350; Asahi Spectra
444 Co., Tokyo, Japan) that was used for illumination of samples in combination with a UV-transmitting
445 filter (UTVAF-50S-36U, SIGMA KOKI, Tokyo, Japan).
446
447 **HPLC analysis**
448 An HPLC analysis was carried out to analyse the conformations of retinal present in the purified
449 pigments. 100 μL of purified pigments were mixed with 210 μL of cold 90% methanol which was
450 stored in −20°C and 30 μL of 1 M hydroxylamine to convert retinal chromophore in a sample into
451 retinal oxime. The retinal oxime was extracted with 700 μL of *n*-hexane. 200 μL of the extract were
452 injected into a YMC-Pack SIL column (particle size 3 μm, 150 × 6.0 mm) and eluted with *n*-hexane
453 containing 15% (v/v) ethyl acetate and 0.15% (v/v) ethanol at a flow rate of 1 mL/min.
454
455 **Bioluminescent reporter assays for Ca^{2+} measurements in cultured cells**

456 Ca^{2+} levels in opsin-expressing cultured cells were assessed by an aequorin-based luminescent assay
457 as described previously (Koyanagi et al., 2022). Briefly, the plasmid containing open reading frames
458 of each opsin was transfected into HEK293S cells in 35 mm dishes by the PEI method with the
459 aequorin plasmid obtained by introducing a reverse mutation A119D into the plasmid
460 [pcDNA3.1+/mit-2mutAEQ] (Addgene no. 45539) (de la Fuente et al., 2012). The transfected
461 HEK293S cells were incubated for ~24 hours at 37°C under 5% CO_2 with the addition of 0.2 μM/dish
462 of 11-*cis* retinal 4 ~ 5 hours after the transfection. Before the luminescence measurements, the culture
463 medium was replaced with a medium containing Coelenterazine *h*, and the cells were incubated to
464 equilibrate with the media at 25°C for at least 2 hours. Dishes of cells were then stimulated with light
465 and luminescence values were recorded using GloMax 20/20n Luminometer (Promega). A green (495
466 nm) LED light (colour: "Cyan", Ex-DHC; BioTools Inc., Gunma, Japan) and arrayed LEDs on a board
467 with spectral emission peaks at 390 nm and 510 nm (SPL-25-CC; REVOX Inc., Kanagawa, Japan)
468 were used as light sources.
469
470 **Computational modelling and QM/MM calculations**
471 The three-dimensional structure of Antho2a was predicted from the primary amino acid sequence
472 using AlphaFold2 (Jumper et al., 2021). The 11-*cis* retinal chromophore linked to the protonated
473 Schiff base was incorporated into the AlphaFold model using as a template the high-resolution
474 structure of bovine rhodopsin solved by time-resolved serial femtosecond X-ray crystallography
475 (Gruhl et al., 2023). A Cl^- anion was initially placed in close proximity to the retinal protonated Schiff
476 base, as observed in the microbial chloride-pump halorhodopsin (Mous et al., 2022). Water molecules
477 were added using HomolWat (Mayol et al., 2020). We determined the pK_a values of the titratable
478 amino acid residues at pH 6.5 using the PROPKA program (Olsson et al., 2011; Søndergaard et al.,
479 2011) and subsequently, the protein was protonated using the tleap program in the AMBER software
480 package (Case et al., 2016). The geometry of this initial model was first relaxed by molecular
481 mechanics energy minimisation with the Amber ff14SB force field (Maier et al., 2015) using steepest
482 descent for 10,000 steps before switching to a conjugate gradient minimiser for an additional 10,000

483 steps. During energy minimisation, a positional restraint of 10 kcal $mol^{-1}Å^{-2}$ was applied to all atoms,
484 including hydrogens. The SHAKE algorithm (Ryckaert et al., 1977) was used to constrain the motion
485 of bonds involving hydrogen. Finally, the geometry of the system was optimised using hybrid
486 quantum mechanics/molecular mechanics (QM/MM) calculations without considering any external
487 environment and with the backbone of the protein frozen (Mroginski et al., 2021; Senn and Thiel,
488 2009). The QM part consists of the retinal chromophore linked to the lysine sidechain cut between the
489 Cδ and Cε atoms forming the protonated Schiff base, along with Cl^-, Glu292 and Ser186. The
490 hydrogen link atom (HLA) scheme was used at the QM/MM boundary. The QM part was treated using
491 the BP86-D3 (BJ) functional (Becke, 1988; Grimme et al., 2011) in conjunction with the cc-pVDZ
492 basis set (Dunning, 1989) and the def2/J auxiliary basis set for the resolution of identity (RI)
493 (Weigend, 2008). The Chain of Spheres exchange (COSX) algorithm was utilised in combination with
494 the resolution of identity for the Coulomb term (RI-J). The rest of the protein was treated with the
495 Amber ff14SB force field. Water molecules were treated with the TIP3P model(Jorgensen et al., 1983).
496 The QM/MM calculations were performed using the quantum chemistry program Orca 5.0.2 (Neese,
497 2022) interfaced with the DL_POLY module of the ChemShell 3.7.1 software package (Metz et al.,
498 2014; Sherwood et al., 2003). The optimised ground state geometries and partial charges were used to
499 calculate the vertical excitation energies using the simplified time-dependent density functional theory
500 (sTD-DFT) (Bannwarth and Grimme, 2014; Runge and Gross, 1984) at the CAM-B3LYP/cc-pVTZ
501 level of theory (Dunning, 1989; Yanai et al., 2004) using the Orca program. The excitation energies
502 were also calculated using the RI-ADC(2) method (Hättig, 2005) with frozen core orbitals and the cc-
503 pVTZ basis set in association with the corresponding auxiliary basis by utilising the Turbomole 7.5.1
504 program package (Furche et al., 2014). The three-dimensional models were visualised using the
505 molecular graphics program PyMOL 2.5.5.

Acknowledgements

We thank Dr. Robert S. Molday (University of British Columbia) for kindly supplying rho 1D4-producing hybridoma. We thank Dr. Masayuki Hatta (Ochanomizu University) for coral sampling. This work was supported by the Japanese Ministry of Education, Culture, Sports, Science and Technology Grants-in-Aid for Scientific Research 23H02516 (to AT), 22H02663 (to MK) and JP20J01841 (YS); and Japan Science and Technology Agency (JST) Core Research for Evolutional Science and Technology (CREST) Grant JPMJCR1753 (to AT). YS was supported by Grant-in-Aid for JSPS Fellows. This work has also been supported by the Swiss National Science Foundation (project grant 192780 to XD) and by the European Union's Horizon 2020 research and innovation programme (grant agreement 951644 to GFXS and Marie Skłodowska-Curie grant agreement 884104 (PSI-FELLOW-III-3i) to SS). We finally thank the members of the High-Performance Computing and Emerging Technologies (HPCE) group at the Paul Scherrer Institute for technical support and assistance with high-performance computing.

Author contributions: YS, MK, and AT conceptualised the study; YS, MK, GFXS, XD, and AT designed the study; YS, TS, YK, and MI performed the experiments and analyses; SS and XD performed the computational modelling; YS and AT wrote the original draft with inputs from SS and XD; All authors reviewed the manuscript and gave final approval for the manuscript.

Competing interests: The authors declare that they have no competing interests.

Data and materials availability: The cDNA sequences of Acropora tenuis opsins in this paper are available in GenBank: eight Cnidopsins (accession no. LC844924–LC844931), seven opsins in the ASO-II group (accession no. LC844932–LC844938), and one opsin in the ASO-I group (accession no. LC844939). All data needed to evaluate the conclusion in this paper are present in the paper and the Supplementary Materials. Additional data related to this paper may be requested from the authors.

References

Agostini S, Suzuki Y, Higuchi T, Casareto BE, Yoshinaga K, Nakano Y, Fujimura H. 2012. Biological and chemical characteristics of the coral gastric cavity. *Coral Reefs* **31**:147–156. doi:10.1007/s00338-011-0831-6

Al-Horani FA, Al-Moghrabi SM, de Beer D. 2003. The mechanism of calcification and its relation to photosynthesis and respiration in the scleractinian coral *Galaxea fascicularis*. *Marine Biology* **142**:419–426. doi:10.1007/s00227-002-0981-8

Bannwarth C, Grimme S. 2014. A simplified time-dependent density functional theory approach for electronic ultraviolet and circular dichroism spectra of very large molecules. *Computational and Theoretical Chemistry* **1040–1041**:45–53. doi:10.1016/j.comptc.2014.02.023

Barott KL, Barron ME, Tresguerres M. 2017. Identification of a molecular pH sensor in coral. *Proceedings of the Royal Society B* **284**:20171769. doi:10.1098/rspb.2017.1769

Becke AD. 1988. Density-functional exchange-energy approximation with correct asymptotic behavior. *Physical Review A* **38**:3098–3100. doi:10.1103/PhysRevA.38.3098

Besaw JE, Ou W-L, Morizumi T, Eger BT, Sanchez Vasquez JD, Chu JHY, Harris A, Brown LS, Miller RJD, Ernst OP. 2020. The crystal structures of a chloride-pumping microbial rhodopsin and its proton-pumping mutant illuminate proton transfer determinants. *Journal of Biological Chemistry* **295**:14793–14804. doi:10.1074/jbc.RA120.014118

Besaw JE, Reichenwallner J, De Guzman P, Tucs A, Kuo A, Morizumi T, Tsuda K, Sljoka A, Miller RJD, Ernst OP. 2022. Low pH structure of heliorhodopsin reveals chloride binding site and intramolecular signaling pathway. *Scientific Reports* **12**:13955. doi:10.1038/s41598-022-17716-9

Cai W-J, Ma Y, Hopkinson BM, Grottoli AG, Warner ME, Ding Q, Hu X, Yuan X, Schoepf V, Xu H, Han C, Melman TF, Hoadley KD, Pettay DT, Matsui Y, Baumann JH, Levas S, Ying Y, Wang Y. 2016. Microelectrode characterization of coral daytime interior pH and carbonate chemistry. *Nature Communications* **7**:11144. doi:10.1038/ncomms11144

Capella-Gutiérrez S, Silla-Martínez JM, Gabaldón T. 2009. trimAl: a tool for automated alignment trimming in large-scale phylogenetic analyses. *Bioinformatics* **25**:1972–1973. doi:10.1093/bioinformatics/btp348

Case DA, Betz RM, Cerutti DS, Cheatham TE III, Darden TA, Duke RE, Giese TJ, Gohlke H, Goetz AW, Homeyer N, Izadi S, Janowski P, Kaus J, Kovalenko A, Lee TS, LeGrand S, Li P, Lin C, Luchko T, Luo R, Madej B, Mermelstein D, Merz KM, Monard G, Nguyen H, Nguyen HT, Omelyan I, Onufriev A, Roe DR, Roitberg A, Sagui C, Simmerling CL, Botello-Smith WM, Swails J, Walker RC, Wang J, Wolf RM, Wu X, Xiaoand L, Kollman PA. 2016. AMBER 2016. San Francisco: University of California.

Church JR, Olsen JMH, Schapiro I. 2021. The impact of retinal configuration on the protein-chromophore interactions in bistable jumping spider rhodopsin-1. *Molecules* **27**:71. doi:10.3390/molecules27010071

Darriba D, Posada D, Kozlov AM, Stamatakis A, Morel B, Flouri T. 2020. ModelTest-NG: a new and scalable tool for the selection of DNA and protein evolutionary models. *Molecular Biology and Evolution* **37**:291–294. doi:10.1093/molbev/msz189

de la Fuente S, Fonteriz RI, de la Cruz PJ, Montero M, Alvarez J. 2012. Mitochondrial free [Ca^{2+}] dynamics measured with a novel low-Ca^{2+} affinity aequorin probe. *Biochemical Journal* **445**:371–376. doi:10.1042/BJ20120423

Dryja TP, Berson EL, Rao VR, Oprian DD. 1993. Heterozygous missense mutation in the rhodopsin gene as a cause of congenital stationary night blindness. *Nature Genetics* **4**:280–283. doi:10.1038/ng0793-280

Dunning TH Jr. 1989. Gaussian basis sets for use in correlated molecular calculations. I. The atoms boron through neon and hydrogen. *The Journal of Chemical Physics* **90**:1007–1023. doi:10.1063/1.456153

Feuda R, Hamilton SC, Mclnerney JO, Pisani D. 2012. Metazoan opsin evolution reveals a simple route to animal vision. *PNAS* **109**:18868–18872. doi:10.1073/pnas.1305990110

Foo SA, Liddell L, Grossman A, Caldeira K. 2020. Photo-movement in the sea anemone Aiptasia influenced by light quality and symbiotic association. *Coral Reefs* **39**:47–54. doi:10.1007/s00338-019-01866-w

Furche F, Ahlrichs R, Hättig C, Klopper W, Sierka M, Weigend F. 2014. Turbomole. *WIREs Computational Molecular Science* **4**:91–100. doi:10.1002/wcms.1162

Gerrard E, Mutt E, Nagata T, Koyanagi M, Flock T, Lesca E, Schertler GFX, Terakita A, Deupi X, Lucas RJ. 2018. Convergent evolution of tertiary structure in rhodopsin visual proteins from vertebrates and box jellyfish. *PNAS* **115**:6201–6206. doi:10.1073/pnas.1721333115

Gornik SG, Bergheim BG, Morel B, Stamatakis A, Foulkes NS, Guse A. 2020. Photoreceptor diversification accompanies the evolution of Anthozoa. *Molecular Biology and Evolution* **38**:1744–1760. doi:10.1093/molbev/msaa304

Grimme S, Ehrlich S, Goerigk L. 2011. Effect of the damping function in dispersion corrected density functional theory. *Journal of Computational Chemistry* **32**:1456–1465. doi:10.1002/jcc.21759

Gruhl T, Weinert T, Rodrigues MJ, Milne CJ, Ortolani G, Nass K, Nango E, Sen S, Johnson PJM, Cirelli C, Furrer A, Mous S, Skopintsev P, James D, Dworkowski F, Båth P, Kekilli D, Ozerov D, Tanaka R, Glover H, Bacellar C, Brünle S, Casadei CM, Diethelm AD, Gashi D, Gotthard G, Guixà-González R, Joti Y, Kabanova V, Knopp G, Lesca E, Ma P, Martiel I, Mühle J, Owada S, Pamula F, Sarabi D, Tejero O, Tsai C-J, Varma N, Wach A, Boutet S, Tono K, Nogly P, Deupi X, Iwata S, Neutze R, Standfuss J, Schertler G, Panneels V. 2023. Ultrafast structural changes direct the first molecular events of vision. *Nature* **615**:939–944. doi:10.1038/s41586-023-05863-6

Hättig C. 2005. Structure optimizations for excited states with correlated second-order methods: CC2 and ADC(2) In: Jensen HJÅ, editor. Response Theory and Molecular Properties (A Tribute to Jan Linderberg and Poul Jørgensen), Advances in Quantum Chemistry. Elsevier. pp. 37–60. doi:10.1016/s0065-3276(05)50003-0

Hering L, Mayer G. 2014. Analysis of the opsin repertoire in the tardigrade *Hypsibius dujardini* provides insights into the evolution of opsin genes in Panarthropoda. *Genome Biology and Evolution* **6**:2380–2391. doi:10.1093/gbe/evu193

Hofmann KP, Scheerer P, Hildebrand PW, Choe HW, Park JH, Heck M, Ernst OP. 2009. A G protein-coupled receptor at work: the rhodopsin model. *Trends in Biochemical Sciences* **34**:540–552. doi:10.1016/j.tibs.2009.07.005

Hosaka T, Yoshizawa S, Nakajima Y, Ohsawa N, Hato M, DeLong EF, Kogure K, Yokoyama S, Kimura-Someya T, Iwasaki W, Shirouzu M. 2016. Structural mechanism for light-driven transport by a new type of chloride ion pump, *Nonlabens marinus* rhodopsin-3. *Journal of Biological Chemistry* **291**:17488–17495. doi:10.1074/jbc.M116.728220

Jin S, Cornwall MC, Oprian DD. 2003. Opsin activation as a cause of congenital night blindness. *Nature Neuroscience* **6**:731–735. doi:10.1038/nn1070

Jorgensen WL, Chandrasekhar J, Madura JD, Impey RW, Klein ML. 1983. Comparison of simple potential functions for simulating liquid water. *The Journal of Chemical Physics* **79**:926–935. doi:10.1063/1.445869

Jumper J, Evans R, Pritzel A, Green T, Figurnov M, Ronneberger O, Tunyasuvunakool K, Bates R, Žídek A, Potapenko A, Bridgland A, Meyer C, Kohl SAA, Ballard AJ, Cowie A, Romera-Paredes B, Nikolov S, Jain R, Adler J, Back T, Petersen S, Reiman D, Clancy E, Zielinski M, Steinegger M, Pacholska M, Berghammer T, Bodenstein S, Silver D, Vinyals O, Senior AW, Kavukcuoglu K, Kohli P, Hassabis D. 2021. Highly accurate protein structure prediction with AlphaFold. *Nature* **596**:583–589. doi:10.1038/s41586-021-03819-2

Katoh K, Standley DM. 2013. MAFFT multiple sequence alignment software version 7: improvements in performance and usability. *Molecular Biology and Evolution* **30**:772–780. doi:10.1093/molbev/mst010

Kayada S, Hisatomi O, Tokunaga F. 1995. Cloning and expression of frog rhodopsin cDNA. *Comparative Biochemistry and Physiology Part B* **110**:599–604. doi:10.1016/0305-0491(94)00179-x

Kishimoto M, Gornik SG, Foulkes NS, Guse A. 2023. Negative phototaxis in the photosymbiotic sea anemone Aiptasia as a potential strategy to protect symbionts from photodamage. *Scientific Reports* **13**:17857. doi:10.1038/s41598-023-44583-9

Kolbe M, Besir H, Essen LO, Oesterhelt D. 2000. Structure of the light-driven chloride pump halorhodopsin at 1.8 Å resolution. *Science* **288**:1390–1396. doi:10.1126/science.288.5470.1390

Koyanagi M, Shen B, Nagata T, Sun L, Wada S, Kamimura S, Kage-Nakadai E, Terakita A. 2022. High-performance optical control of GPCR signaling by bistable animal opsins MosOpn3 and LamPP in a molecular property-dependent manner. *PNAS* **119**:e2204341119. doi:10.1073/pnas.2204341119

Koyanagi M, Takano K, Tsukamoto H, Ohtsu K, Tokunaga F, Terakita A. 2008. Jellyfish vision starts with cAMP signaling mediated by opsin-G_s cascade. *PNAS* **105**:15576–15580. doi:10.1073/pnas.0806215105

Koyanagi M, Terakita A. 2014. Diversity of animal opsin-based pigments and their optogenetic potential. *Biochimica et Biophysica Acta* **1837**:710–716. doi:10.1016/j.bbabio.2013.09.003

Kozlov AM, Darriba D, Flouri T, Morel B, Stamatakis A. 2019. RAxML-NG: a fast, scalable and user-friendly tool for maximum likelihood phylogenetic inference. *Bioinformatics* **35**:4453–4455. doi:10.1093/bioinformatics/btz305

Kozmik Z, Ruzickova J, Jonasova K, Matsumoto Y, Vopalensky P, Kozmikova I, Strnad H, Kawamura S, Piatigorsky J, Paces V, Vlcek C. 2008. Assembly of the cnidarian camera-type eye from vertebrate-like components. *PNAS* **105**:8989–8993. doi:10.1073/pnas.0800388105

Levy S, Elek A, Grau-Bové X, Menéndez-Bravo S, Iglesias M, Tanay A, Mass T, Sebé-Pedrós A. 2021. A stony coral cell atlas illuminates the molecular and cellular basis of coral symbiosis, calcification, and immunity. *Cell* **184**:2973–2987. doi:10.1016/j.cell.2021.04.005

Maier JA, Martinez C, Kasavajhala K, Wickstrom L, Hauser KE, Simmerling C. 2015. Ff14SB: improving the accuracy of protein side chain and backbone parameters from ff99SB. *Journal of Chemical Theory and Computation* **11**:3696–3713. doi:10.1021/acs.jctc.5b00255

Mason BM, Koyanagi M, Sugihara T, Iwasaki M, Slepak V, Miller DJ, Sakai Y, Terakita A. 2023. Multiple opsins in a reef-building coral, *Acropora millepora*. *Scientific Reports* **13**:1628. doi:10.1038/s41598-023-28476-5

Mayol E, García-Recio A, Tiemann JKS, Hildebrand PW, Guixà-González R, Olivella M, Cordomí A. 2020. HomolWat: a web server tool to incorporate ‘homologous’ water molecules into GPCR structures. *Nucleic Acids Research* **48**:W54–W59. doi:10.1093/nar/gkaa440

Metz S, Kästner J, Sokol AA, Keal TW, Sherwood P. 2014. ChemShell—a modular software package for QM/MM simulations. *WIREs Computational Molecular Science* **4**:101–110. doi:10.1002/wcms.1163

Mous S, Gotthard G, Ehrenberg D, Sen S, Weinert T, Johnson PJM, James D, Nass K, Furrer A, Kekilli D, Ma P, Brünle S, Casadei CM, Martiel I, Dworkowski F, Gashi D, Skopintsev P, Wranik M, Knopp G, Panepucci E, Panneels V, Cirelli C, Ozerov D, Schertler GFX, Wang M, Milne C, Standfuss J, Schapiro I, Heberle J, Nogly P. 2022. Dynamics and mechanism of a light-driven chloride pump. *Science* **375**:845–851. doi:10.1126/science.abj6663

Mroginski M-A, Adam S, Amoyal GS, Barnoy A, Bondar A-N, Borin VA, Church JR, Domratcheva T, Ensing B, Fanelli F, Ferré N, Filiba O, Pedraza-González L, González R, González-Espinoza CE, Kar RK, Kemmler L, Kim SS, Kongsted J, Krylov AI, Lahav Y, Lazaratos M, NasserEddin Q, Navizet I, Nemukhin A, Olivucci M, Olsen JMH, Pérez de Alba Ortíz A, Pieri E, Rao AG, Rhee YM, Ricardi N, Sen S, Solov’yov IA, De Vico L, Wesolowski TA, Wiebeler C, Yang X, Schapiro I. 2021. Frontiers in multiscale modeling of photoreceptor proteins. *Photochemistry and Photobiology* **97**:243–269. doi:10.1111/php.13372

Nagata T, Koyanagi M, Tsukamoto H, Mutt E, Schertler GFX, Deupi X, Terakita A. 2019. The counterion–retinylidene Schiff base interaction of an invertebrate rhodopsin rearranges upon light activation. *Communications Biology* **2**:180. doi:10.1038/s42003-019-0409-3

Nathans J. 1990. Determinants of visual pigment absorbance: identification of the retinylidene Schiff’s base counterion in bovine rhodopsin. *Biochemistry* **29**:9746–9752. doi:10.1021/bi00493a034

Neese F. 2022. Software update: the ORCA program system—version 5.0. *WIREs Computational Molecular Science* **12**. doi:10.1002/wcms.1606

Olsson MHM, Søndergaard CR, Rostkowski M, Jensen JH. 2011. PROPKA3: consistent treatment of internal and surface residues in empirical pKa predictions. *Journal of Chemical Theory and Computation* **7**:525–537. doi:10.1021/ct100578z

Picciani N, Kerlin JR, Sierra NC, Swafford AJM, Ramirez MD, Cannon JT, Daly M, Oakley TH. 2018. Prolific origination of eyes in cnidaria with co-option of non-visual opsins. *Current Biology* **28**:2413-2419.e4. doi:10.2139/ssrn.3155889

Pitt GA, Collins FD, Morton RA, Stok P. 1955. Studies on rhodopsin. VIII. Retinylidenemethylamine, an indicator yellow analogue. *Biochemical Journal* **59**:122–128. doi:10.1042/bj0590122

Ramirez MD, Pairett AN, Pankey MS, Serb JM, Speiser DI, Swafford AJ, Oakley TH. 2016. The last common ancestor of most bilaterian animals possessed at least nine opsins. *Genome Biology and Evolution* **8**:3640–3652. doi:10.1093/gbe/evw248

Ridge KD, Abdulaev NG. 2000. Folding and assembly of rhodopsin from expressed fragments. *Methods in Enzymology* **315**:59–70. doi:10.1016/s0076-6879(00)15834-3

Runge E, Gross EKU. 1984. Density-functional theory for time-dependent systems. *Physical Review Letters* **52**:997–1000. doi:10.1103/physrevlett.52.997

Ryckaert J-P, Ciccotti G, Berendsen HJC. 1977. Numerical integration of the cartesian equations of motion of a system with constraints: molecular dynamics of n-alkanes. *Journal of Computational Physics* **23**:327–341. doi:10.1016/0021-9991(77)90098-5

Sakai K, Ikeuchi H, Fujiyabu C, Imamoto Y, Yamashita T. 2022. Convergent evolutionary counterion displacement of bilaterian opsins in ciliary cells. *Cellular and Molecular Life Sciences* **79**:493. doi:10.1007/s00018-022-04525-6

Sakmar TP, Franke RR, Khorana HG. 1991. The role of the retinylidene Schiff base counterion in rhodopsin in determining wavelength absorbance and Schiff base pK_a. *PNAS* **88**:3079–3083. doi:10.1073/pnas.88.8.3079

Sakmar TP, Franke RR, Khorana HG. 1989. Glutamic acid-113 serves as the retinylidene Schiff base counterion in bovine rhodopsin. *PNAS* **86**:8309–8313. doi:10.1073/pnas.86.21.8309

Senn HM, Thiel W. 2009. QM/MM methods for biomolecular systems. *Angewandte Chemie International Edition* **48**:1198–1229. doi:10.1002/anie.200802019

Sherwood P, de Vries AH, Guest MF, Schreckenbach G, Catlow CRA, French SA, Sokol AA, Bromley ST, Thiel W, Turner AJ, Billeter S, Terstegen F, Thiel S, Kendrick J, Rogers SC, Casci J, Watson M, King F, Karlsen E, Sjøvoll M, Fahmi A, Schäfer A, Lennartz C. 2003. QUASI: a general purpose implementation of the QM/MM approach and its application to problems in catalysis. *Journal of Molecular Structure:THEOCHEM* **632**:1–28. doi:10.1016/s0166-1280(03)00285-9

Shichida Y, Kato T, Sasayama S, Fukada Y, Yoshizawa T. 1990. Effects of chloride on chicken iodopsin and the chromophore transfer reactions from iodopsin to scotopsin and B-photopsin. *Biochemistry* **29**:5843–5848. doi:10.1021/bi00476a028

Shihoya W, Inoue K, Singh M, Konno M, Hososhima S, Yamashita K, Ikeda K, Higuchi A, Izume T, Okazaki S, Hashimoto M, Mizutori R, Tomida S, Yamauchi Y, Abe-Yoshizumi R, Katayama K, Tsunoda SP, Shibata M, Furutani Y, Pushkarev A, Béjà O, Uchihashi T, Kandori H, Nureki O. 2019. Crystal structure of heliorhodopsin. *Nature* **574**:132–136. doi:10.1038/s41586-019-1604-6

Shinzato C, Khalturin K, Inoue J, Zayasu Y, Kanda M, Kawamitsu M, Yoshioka Y, Yamashita H, Suzuki G, Satoh N. 2020. Eighteen coral genomes reveal the evolutionary origin of Acropora strategies to accommodate environmental changes. *Molecular Biology and Evolution* **38**:16–30. doi:10.1093/molbev/msaa216

Søndergaard CR, Olsson MHM, Rostkowski M, Jensen JH. 2011. Improved treatment of ligands and coupling effects in empirical calculation and rationalization of pK_a values. *Journal of Chemical Theory and Computation* **7**:2284–2295. doi:10.1021/ct200133y

Steinberg G, Ottolenghi M, Sheves M. 1993. pK_a of the protonated Schiff base of bovine rhodopsin. A study with artificial pigments. *Biophysical Journal* **64**:1499–1502. doi:10.1016/S0006-3495(93)81518-2

Suga H, Schmid V, Gehring WJ. 2008. Evolution and functional diversity of jellyfish opsins. *Current Biology* **18**:51–55. doi:10.1016/j.cub.2007.11.059

Terakita A. 2005. The opsins. *Genome Biology* **6**:213. doi:10.1186/gb-2005-6-3-213

Terakita A, Kawano-Yamashita E, Koyanagi M. 2012. Evolution and diversity of opsins. *Wiley Interdisciplinary Reviews: Membrane Transport and Signaling* **1**:104–111. doi:10.1002/wmts.6

Terakita A, Koyanagi M, Tsukamoto H, Yamashita T, Miyata T, Shichida Y. 2004. Counterion displacement in the molecular evolution of the rhodopsin family. *Nature Structural and Molecular Biology* **11**:284–289. doi:10.1038/nsmb731

Terakita A, Yamashita T, Shichida Y. 2000. Highly conserved glutamic acid in the extracellular IV–V loop in rhodopsins acts as the counterion in retinochrome, a member of the rhodopsin family. *PNAS* **97**:14263–14267. doi:10.1073/pnas.260349597

Tsutsui K, Shichida Y. 2010. Photosensitivities of rhodopsin mutants with a displaced counterion. *Biochemistry* **49**:10089–10097. doi:10.1021/bi101020p

Venn AA, Tambutté E, Lotto S, Zoccola D, Allemand D, Tambutté S. 2009. Imaging intracellular pH in a reef coral and symbiotic anemone. *PNAS* **106**:16574–16579. doi:10.1073/pnas.0902894106

Voolstra C, Miller D, Ragan M, Hoffmann A, Hoegh-Guldberg O, Bourne D, Ball E, Ying H, Foret S, Takahashi S, Weynberg K, van Oppen M, Morrow K, Chan CX, Rosic N, Leggat W, Sprungala S, Imelfort M, Tyson G, Kassahn K, Lundgren P, Beeden R, Ravasi T, Berumen M, Abel E, Fyffe T. 2015. The ReFuGe 2020 Consortium—using “omics” approaches to explore the adaptability and resilience of coral holobionts to environmental change. *Frontiers in Marine Science* **2:**68. doi:10.3389/fmars.2015.00068

Weigend F. 2008. Hartree-Fock exchange fitting basis sets for H to Rn. *Journal of Computational Chemistry* **29**:167–175. doi:10.1002/jcc.20702

Yanai T, Tew DP, Handy NC. 2004. A new hybrid exchange–correlation functional using the Coulomb-attenuating method (CAM-B3LYP). *Chemical Physics Letters* **393**:51–57. doi:10.1016/j.cplett.2004.06.011

Zhukovsky EA, Oprian DD. 1989. Effect of carboxylic acid side chains on the absorption maximum of visual pigments. *Science* **246**:928–930. doi:10.1126/science.2573154

Figures

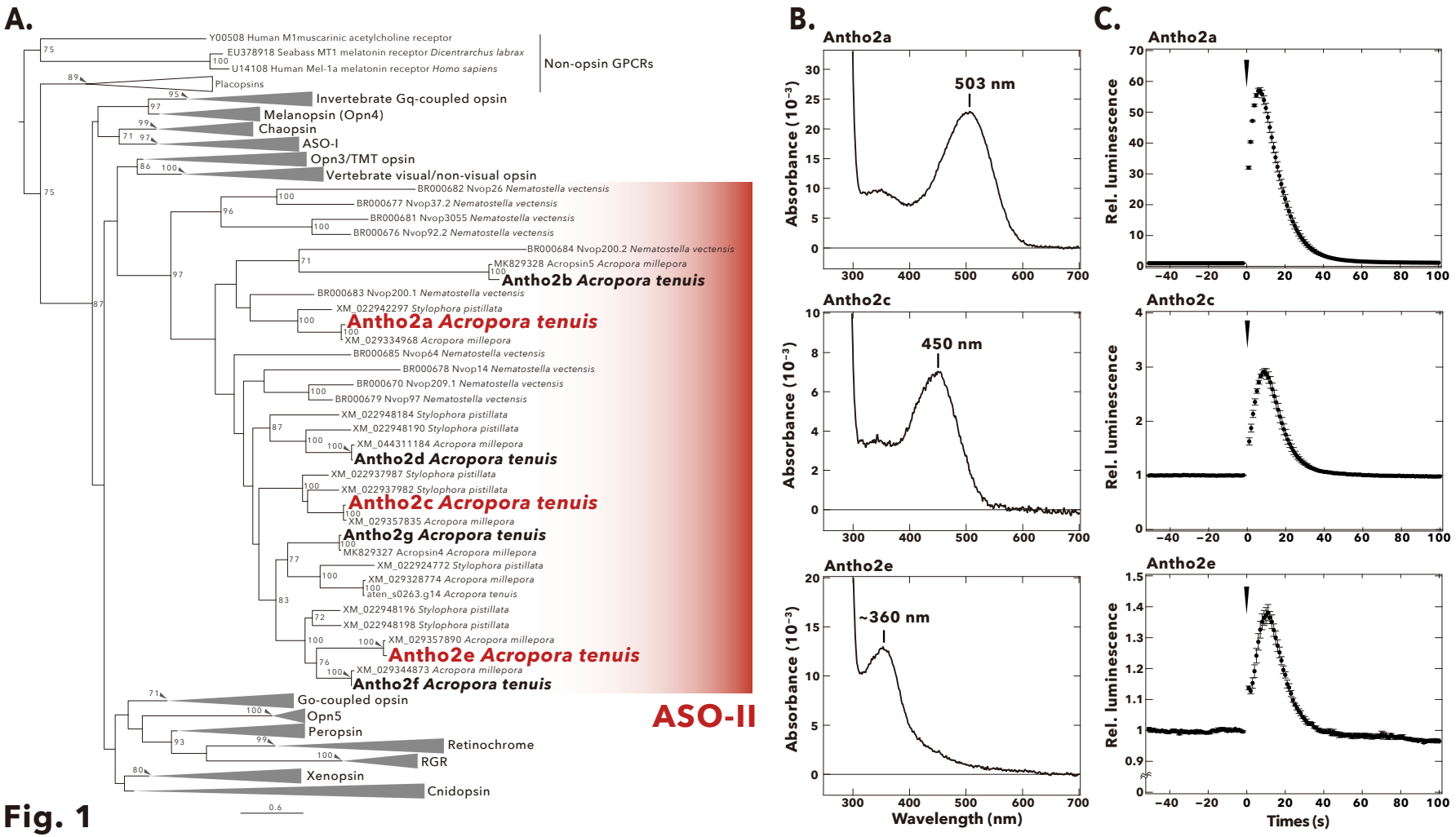

Fig. 1

776 **Fig. 1. Phylogenetic tree, absorption spectra, and light-induced Ca^{2+} responses of *Acropora***
777 ***tenuis* opsins belonging to the ASO-II group. (A)** Maximum-likelihood (ML) tree of animal opsins
778 including *A. tenuis* opsins in the ASO-II group. Seven opsins in the ASO-II group that were identified
779 and cloned from *A. tenuis* in this study are shown in bold and the three members for which we
780 obtained absorption spectra are highlighted in red. Numbers at the nodes represent support values of
781 each ML branch estimated by 1000 bootstrap samplings (≥ 70% are indicated). Scale bar = 0.6
782 substitutions per site. All branches and support values are provided in Fig. S1. **(B)** Absorption spectra
783 in the dark of three *A. tenuis* opsins in the ASO-II group (Antho2a, Antho2c and Antho2e). The
784 absorption spectra were measured at 0°C in 140 mM NaCl at pH 6.5. The number in each graph shows
785 the λ_{max} value. **(C)** Results of the aequorin-based bioluminescent reporter assay for monitoring light-
786 induced changes in Ca^{2+} in HEK293S cells expressing the same three opsins in the ASO-II group as in
787 B. In each graph, luminescence values were normalised to the baseline. Black circles with error bars
788 indicate the means ± SEMs (n = 3) of the measured relative luminescence. Black arrowheads at time 0
789 indicate the timing of one-minute irradiation with green (495 nm; for Antho2a and Antho2c) or UV
790 (395 nm; for Antho2e) light.

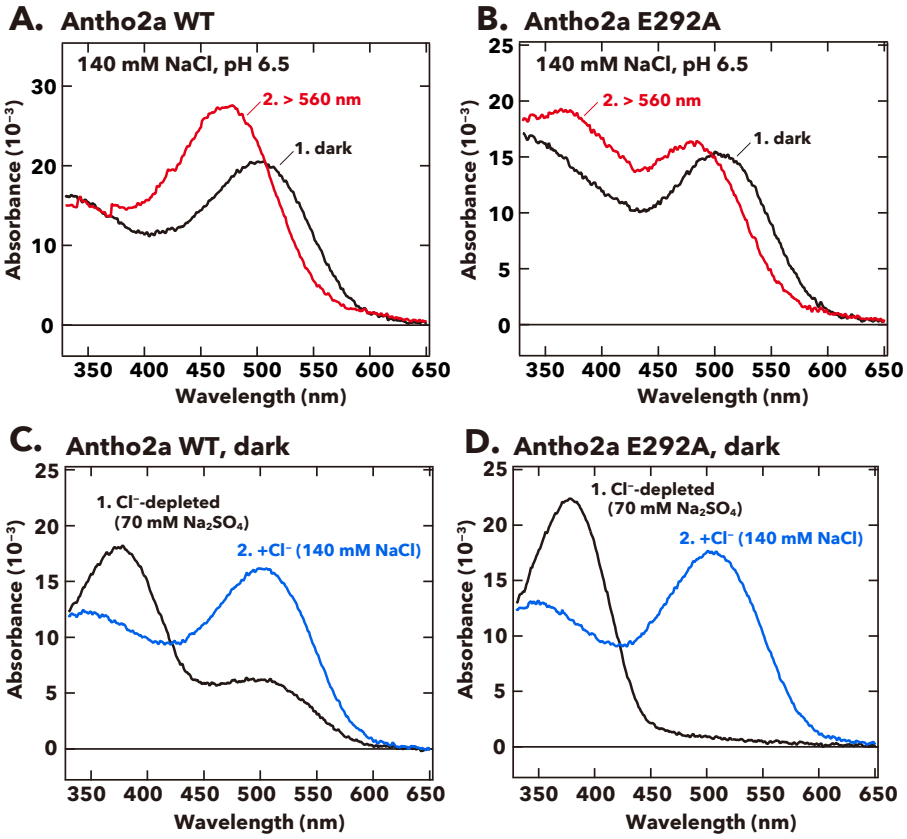

Fig. 2

Fig. 2. Absorption spectra of wild type and the E292A mutant of *A. tenuis* Antho2a. (A, B) Absorption spectra of the dark state (curve 1, black) and the photoproduct (curve 2, red) of the wild type (Antho2a WT, **A**) and the E292A mutant (Antho2a E292A, **B**) at 140 mM NaCl and pH 6.5. The samples were kept at 0°C during the spectroscopic measurements**. (C, D)** Absorption spectra of the dark state of Antho2a WT **(C)** and Antho2a E292A **(D)** prepared in Cl^--depleted conditions, before (curve 1, black) and after (curve 2, blue) adding Cl^- (see Materials and Methods for details). In the Cl^--depleted condition, the pigments were solubilised in 70 mM Na_2SO_4, which reportedly does not access to the Cl^- binding site in the chicken red-sensitive cone visual pigment iodosin (Shichida et al., 1990), to moderate protein denaturation.

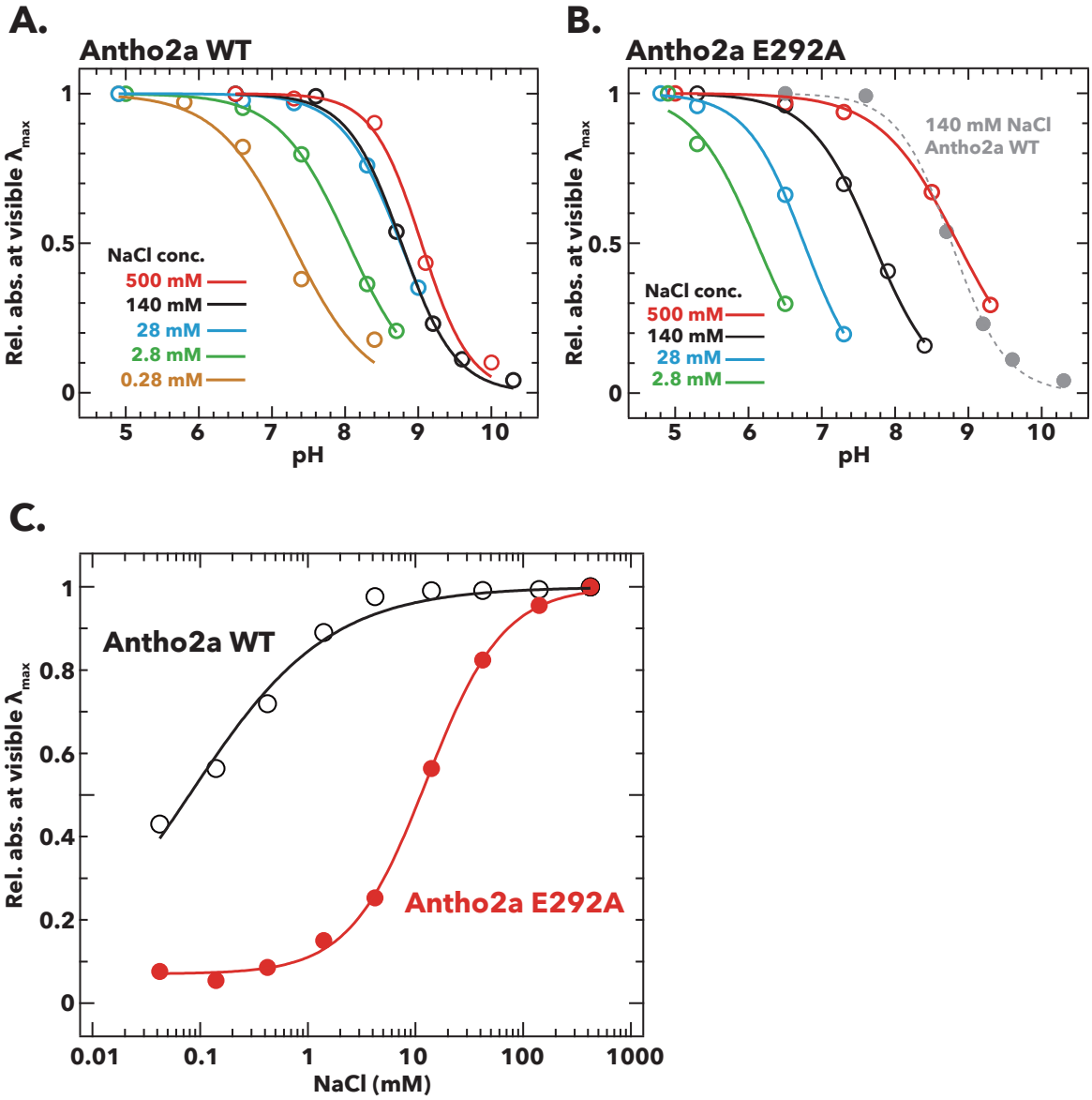

Fig. 3

Fig. 3. Effects of pH and Cl^- concentration on the absorption spectra of the dark states of wild type Antho2a and the Antho2a E292A mutant. (A, B) Changes in the absorbance at λ_{max} as a function of pH for **(A)** wild type Antho2a and **(B)** the E292A mutant at different Cl^- concentrations. The absorbance values at "visible λ_{max}" (mean absorbance at 503 ± 5 nm for the wild type and 505 ± 5 nm for the E292A mutant, respectively) were normalised for each Cl^- concentration to those at the lowest pH, in which the Schiff base is assumed to be fully protonated ("Rel. abs. at visible λ_{max}" in the y-axes). Solid and dashed lines represent sigmoid fits to the experimental data for each Cl^-

809 concentration (indicated by different colours). The pH-dependent change of wild type Antho2a at
810 140mM NaCl is also shown in B (dotted grey line). The full absorption spectra used to generate these
811 plots are provided in Fig. S7 (for wild type Antho2a) and Fig. S9 (for the E292A mutant). **(C)** Changes
812 in the absorbance at λ_{max} for wild type Antho2a (black open circles) and the E292A mutant (red solid
813 circles) as a function of Cl^- concentration. The absorbance values at visible λ_{max} were normalised to
814 those at 500 mM NaCl for both the wild type and the E292A mutant. The lines in the graph were
815 generated by fitting the Hill equation to the experimental data.

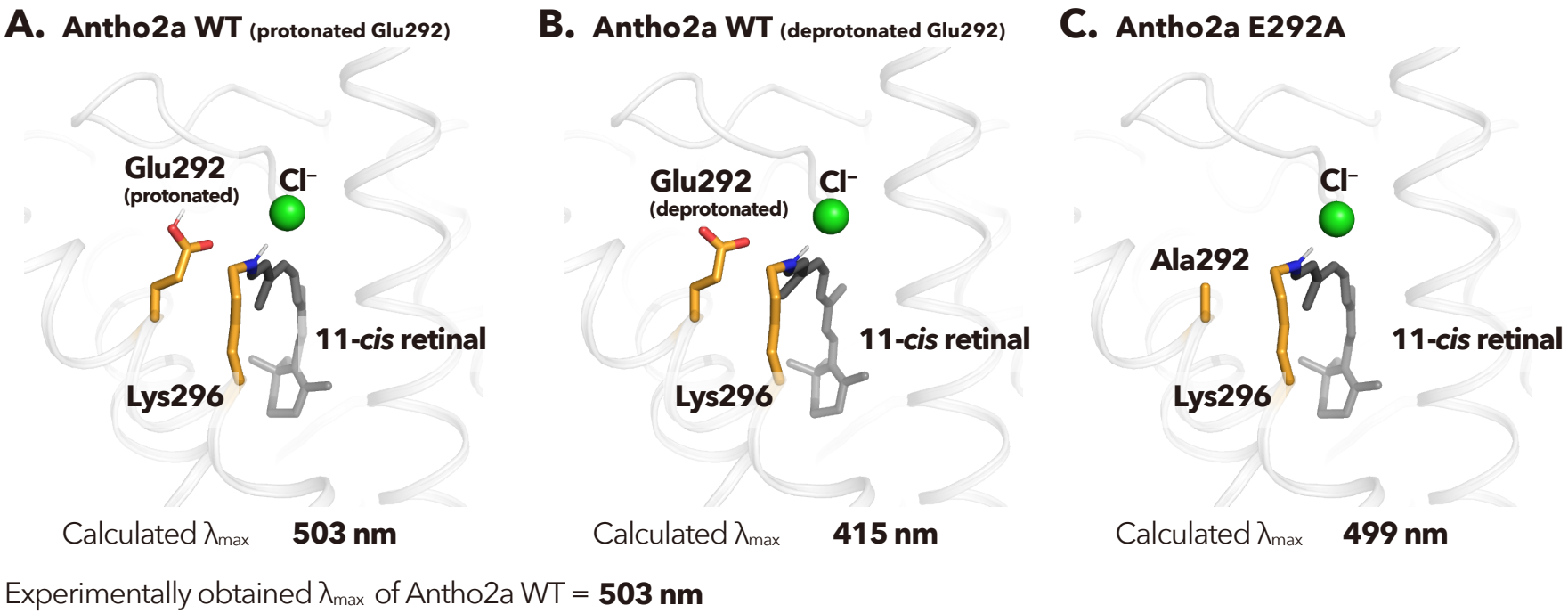

Fig. 4

Fig. 4. Structural models of the retinal binding pocket in the dark state of **(A, B)** wild type Antho2a and **(C)** the E292A mutant obtained using QM/MM calculations. For wild type Antho2a, two models are shown: **(A)** with a protonated (neutral) Glu292 and **(B)** a deprotonated (negatively charged) Glu292.

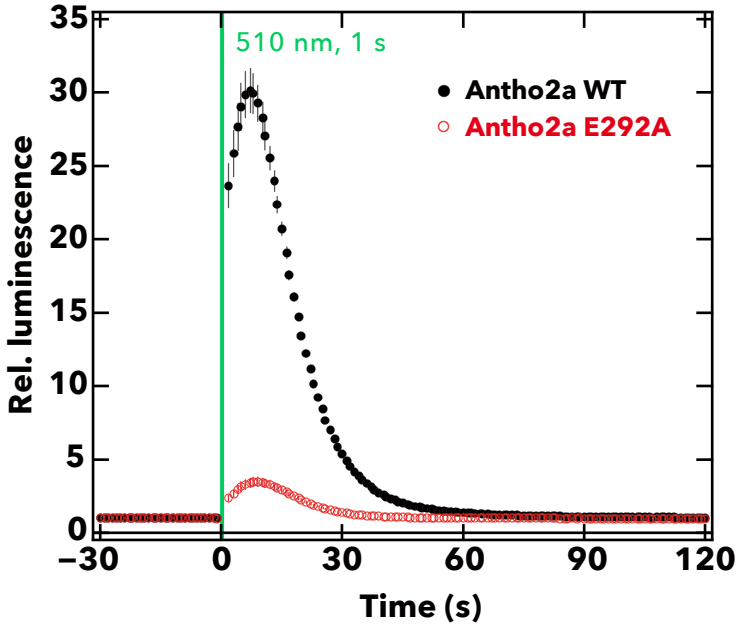

Fig. 5

Fig. 5. Comparison of the light-evoked intracellular Ca^{2+} levels between wild type Antho2a and the E292A mutant. The graph shows the mean ± S.E.M (n = 4) of the measured relative luminescence values (luminescence values normalised to the baseline) for wild type Antho2a (black) and the E292A mutant (red). The green vertical line indicates the time of cell illumination with green light (510 nm, for 1 s, 1.65×10^{15} photons/cm^2/s).

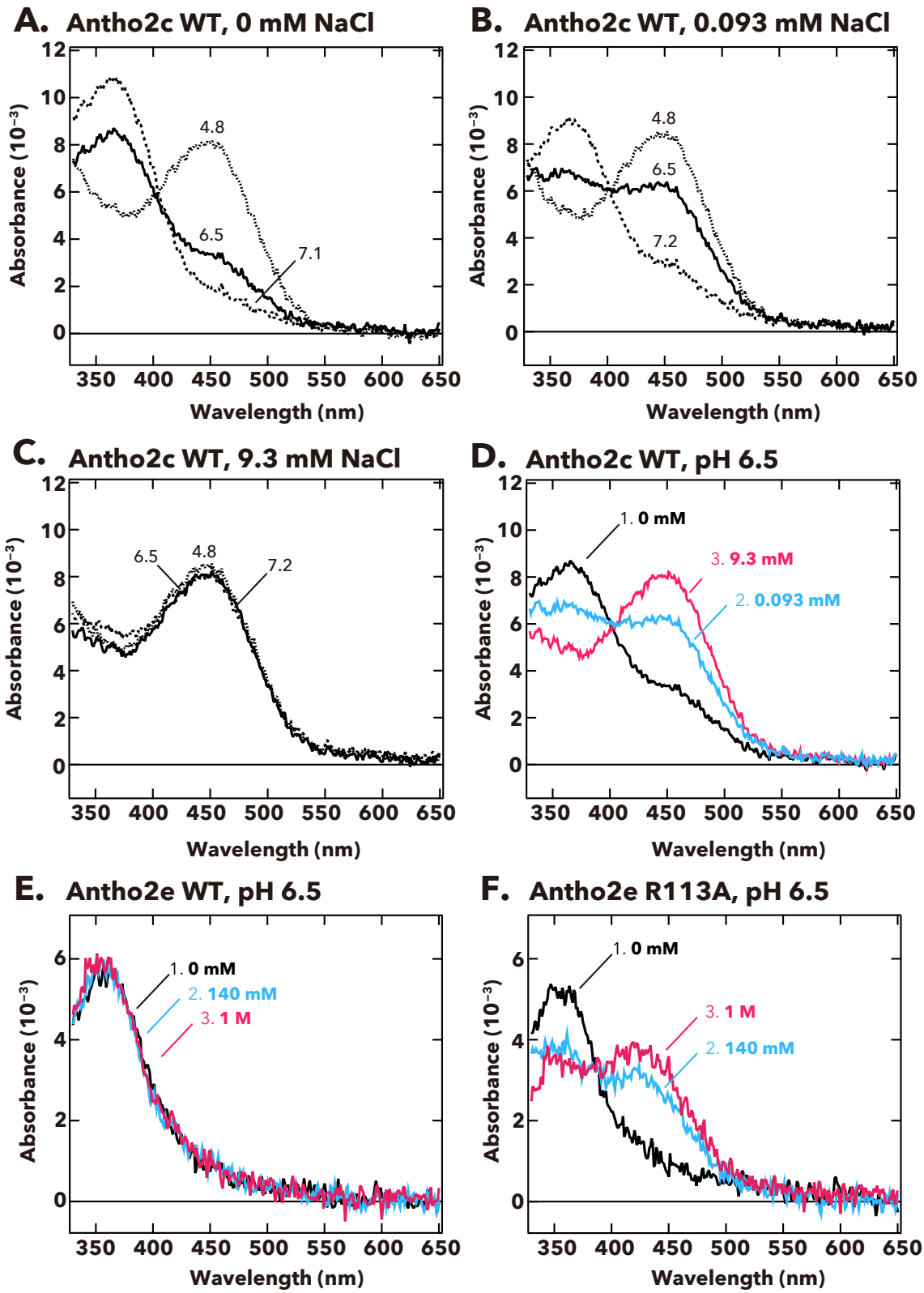
A. Antho2c WT, 0 mM NaCl
B. Antho2c WT, 0.093 mM NaCl
C. Antho2c WT, 9.3 mM NaCl
D. Antho2c WT, pH 6.5
E. Antho2e WT, pH 6.5
F. Antho2e R113A, pH 6.5
Absorbance (10⁻³)
Wavelength (nm)
4.8
6.5
7.1
7.2
1. 0 mM
2. 0.093 mM
3. 9.3 mM
2. 140 mM
3. 1 M

Fig. 6

826

827 **Fig. 6. pH-dependent changes in the absorption spectra of Antho2c and Antho2e at different Cl^-**

828 **concentrations at 0°C. (A–C)** Absorption spectra of purified wild type Antho2c pigment at **(A)** 0

829 mM, **(B)** 0.093 mM, and **(C)** 9.3 mM NaCl concentrations. The corresponding pH values are indicated

830 on each curve in the graphs. **(D)** Summary of the spectral changes for wild type Antho2c across

831 different Cl^- concentrations at neutral pH (pH 6.5). **(E, F)** Absorption spectra of **(E)** wild type Antho2e

832 (Antho2e WT) and **(F)** its R113A mutant (Antho2e R113A) at different Cl^- concentrations at pH 6.5 at

833 0°C. Each colour indicates a different Cl^- concentration.

Supplementary table and figures

Table S1. Vertical excitation energies (ΔE_{calc}) and oscillator strengths (f) computed by quantum mechanics/molecular mechanics (QM/MM) calculations using different QM methods with the cc-pVTZ basis set.

QM Region	**sTD-DFT CAM-B3LYP**		**ADC(2)**	
	ΔE_{calc} nm (eV)	**f**	**ΔE_{calc} nm (eV)**	**f**
RET+Lyr296+Cl+Ser186+**Glu292 (deprotonated)**	415 (2.99)	1.54	374 (3.32)	1.64
RET+Lyr296+Cl+Ser186+**Glu292 (protonated)**	503 (2.47)	1.19	416 (2.98)	1.43
RET+Lyr296+Cl+Ser186+**Ala292**	499 (2.49)	1.19	426 (2.91)	1.36

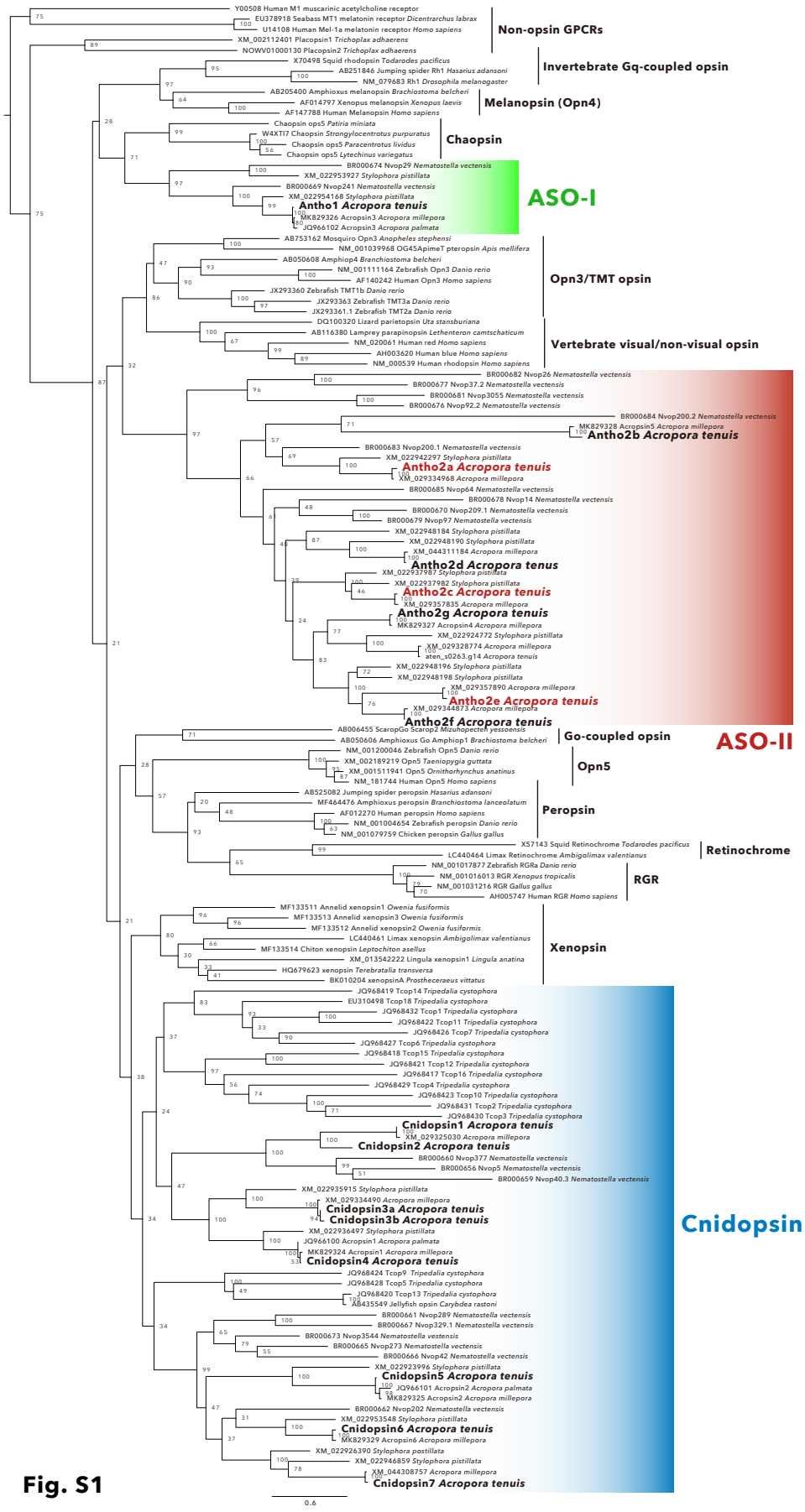
Y00508 Human M1 muscarinic acetylcholine receptor
EU378918 Seabass MT1 melatonin receptor Dicentrarchus labrax
U14108 Human Mel-1a melatonin receptor Homo sapiens
Non-opsin GPCRs
XM_002112401 Placopsin1 Trichoplax adhaerens
NOWV01000130 Placopsin2 Trichoplax adhaerens
X70498 Squid rhodopsin Todarodes pacificus
AB251846 Jumping spider Rh1 Hasarius adansoni
NM_079683 Rh1 Drosophila melanogaster
Invertebrate Gq-coupled opsin
AB205400 Amphioxus melanopsin Brachiostoma belcheri
AF014797 Xenopus melanopsin Xenopus laevis
AF147788 Human Melanopsin Homo sapiens
Melanopsin (Opn4)
Chaopsin ops5 Patiria miniata
W4XTI7 Chaopsin Strongylocentrotus purpuratus
Chaopsin ops5 Paracentrotus lividus
Chaopsin ops5 Lytechinus variegatus
Chaopsin
BR000674 Nvop29 Nematostella vectensis
XM_022953927 Stylophora pistillata
BR000669 Nvop241 Nematostella vectensis
XM_022954148 Stylophora pistillata
Antho1 Acropora tenuis
MK829326 Acropsin3 Acropora millepora
JQ966102 Acropsin3 Acropora palmata
ASO-I
AB753162 Mosquiro Opn3 Anopheles stephensi
NM_001039968 OG45ApimeT pteropsin Apis mellifera
AB050608 Amphiop4 Branchiostoma belcheri
NM_001111164 Zebrafish Opn3 Danio rerio
AF140242 Human Opn3 Homo sapiens
JX293360 Zebrafish TMT1b Danio rerio
JX293363 Zebrafish TMT3a Danio rerio
JX293361.1 Zebrafish TMT2a Danio rerio
Opn3/TMT opsin
DQ100320 Lizard parietopsin Uta stansburiana
AB116380 Lamprey parapinopsin Lethenteron camtschaticum
NM_020061 Human red Homo sapiens
AH003620 Human blue Homo sapiens
NM_000539 Human rhodopsin Homo sapiens
Vertebrate visual/non-visual opsin
BR000682 Nvop26 Nematostella vectensis
BR000677 Nvop37.2 Nematostella vectensis
BR000681 Nvop3055 Nematostella vectensis
BR000676 Nvop92.2 Nematostella vectensis
BR000684 Nvop200.2 Nematostella vectensis
MK829328 Acropsin5 Acropora millepora
Antho2b Acropora tenuis
BR000683 Nvop200.1 Nematostella vectensis
XM_022942297 Stylophora pistillata
Antho2a Acropora tenuis
XM_029334968 Acropora millepora
BR000685 Nvop64 Nematostella vectensis
BR000678 Nvop14 Nematostella vectensis
BR000670 Nvop209.1 Nematostella vectensis
BR000679 Nvop97 Nematostella vectensis
XM_022948184 Stylophora pistillata
XM_022948190 Stylophora pistillata
XM_044311184 Acropora millepora
Antho2d Acropora tenus
XM_022937987 Stylophora pistillata
XM_022937982 Stylophora pistillata
Antho2c Acropora tenuis
XM_029357835 Acropora millepora
Antho2g Acropora tenuis
MK829327 Acropsin4 Acropora millepora
XM_022924772 Stylophora pistillata
XM_029328774 Acropora millepora
aten_s0263.g14 Acropora tenuis
XM_022948196 Stylophora pistillata
XM_022948198 Stylophora pistillata
XM_029357890 Acropora millepora
Antho2e Acropora tenuis
XM_029344873 Acropora millepora
Antho2f Acropora tenuis
ASO-II
AB006455 ScaropGo Scarop2 Mizuhopecten yessoensis
AB050606 Amphioxus Go Amphiop1 Brachiostoma belcheri
Go-coupled opsin
NM_001200046 Zebrafish Opn5 Danio rerio
XM_002189219 Opn5 Taeniopygia guttata
XM_001511941 Opn5 Ornithorhynchus anatinus
NM_181744 Human Opn5 Homo sapiens
Opn5
AB525082 Jumping spider peropsin Hasarius adansoni
MF464476 Amphioxus peropsin Branchiostoma lanceolatum
AF012270 Human peropsin Homo sapiens
NM_001004654 Zebrafish peropsin Danio rerio
NM_001079759 Chicken peropsin Gallus gallus
Peropsin
X57143 Squid Retinochrome Todarodes pacificus
LC440464 Limax Retinochrome Ambigolimax valentianus
Retinochrome
NM_001017877 Zebrafish RGRa Danio rerio
NM_001016013 RGR Xenopus tropicalis
NM_001031216 RGR Gallus gallus
AH005747 Human RGR Homo sapiens
RGR
MF133511 Annelid xenopsin1 Owenia fusiformis
MF133513 Annelid xenopsin3 Owenia fusiformis
MF133512 Annelid xenopsin2 Owenia fusiformis
LC440461 Limax xenopsin Ambigolimax valentianus
MF133514 Chiton xenopsin Leptochiton asellus
XM_013542222 Lingula xenopsin1 Lingula anatina
HQ679623 xenopsin Terebratalia transversa
BK010204 xenopsinA Prostheceraeus vittatus
Xenopsin
JQ968419 Tcop14 Tripedalia cystophora
EU310498 Tcop18 Tripedalia cystophora
JQ968432 Tcop1 Tripedalia cystophora
JQ968422 Tcop11 Tripedalia cystophora
JQ968426 Tcop7 Tripedalia cystophora
JQ968427 Tcop6 Tripedalia cystophora
JQ968418 Tcop15 Tripedalia cystophora
JQ968421 Tcop12 Tripedalia cystophora
JQ968417 Tcop16 Tripedalia cystophora
JQ968429 Tcop4 Tripedalia cystophora
JQ968423 Tcop10 Tripedalia cystophora
JQ968431 Tcop2 Tripedalia cystophora
JQ968430 Tcop3 Tripedalia cystophora
Cnidopsin1 Acropora tenuis
XM_029325030 Acropora millepora
Cnidopsin2 Acropora tenuis
BR000660 Nvop377 Nematostella vectensis
BR000656 Nvop5 Nematostella vectensis
BR000659 Nvop40.3 Nematostella vectensis
XM_022935915 Stylophora pistillata
XM_029334490 Acropora millepora
Cnidopsin3a Acropora tenuis
Cnidopsin3b Acropora tenuis
XM_022936497 Stylophora pistillata
JQ966100 Acropsin1 Acropora palmata
MK829324 Acropsin1 Acropora millepora
Cnidopsin4 Acropora tenuis
JQ968424 Tcop9 Tripedalia cystophora
JQ968428 Tcop5 Tripedalia cystophora
JQ968420 Tcop13 Tripedalia cystophora
AB435549 Jellyfish opsin Carybdea rastoni
BR000661 Nvop289 Nematostella vectensis
BR000667 Nvop329.1 Nematostella vectensis
BR000673 Nvop3544 Nematostella vestensis
BR000665 Nvop273 Nematostella vectensis
BR000666 Nvop42 Nematostella vectensis
XM_022923996 Stylophora pistillata
Cnidopsin5 Acropora tenuis
JQ966101 Acropsin2 Acropora palmata
MK829325 Acropsin2 Acropora millepora
BR000662 Nvop202 Nematostella vectensis
XM_022953548 Stylophora pistillata
Cnidopsin6 Acropora tenuis
MK829329 Acropsin6 Acropora millepora
XM_022926390 Stylophora pastillata
XM_022946859 Stylophora pistillata
XM_044308757 Acropora millepora
Cnidopsin7 Acropora tenuis
Cnidopsin
0.6

Fig. S1

841 **Fig. S1. Maximum-likelihood (ML) tree of animal opsins, with non-opsin GPCRs included as an**
842 **outgroup** (a simplified version of the ML tree is shown in Fig. 1A). The tree includes opsins
843 belonging to the eight main groups (see main text) as well as of opsins from the recently identified
844 subgroups xenopsins and chaopsins[6]. The sixteen *A. tenuis* opsins (eight opsins in the cnidopsin group,
845 one opsin in the ASO-I group, and seven opsins in the ASO-II group) that were identified in this study
846 are shown in bold. The three opsins in the ASO-II group for which absorption spectra were
847 successfully obtained are highlighted in red. Numbers at nodes represent support values for the ML
848 branch estimated by 1000 bootstrap samplings (≥ 70% are indicated). Scale bar = 0.6 substitutions per
849 site.

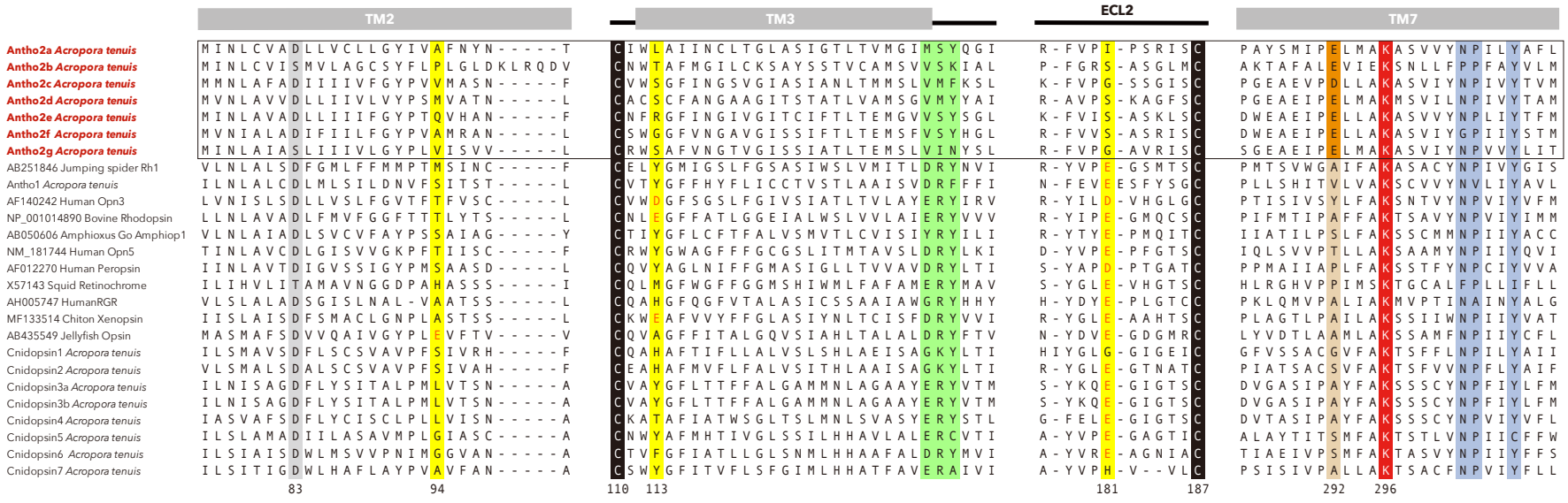

Fig. S2

Fig. S2. Amino acid sequence alignment of opsins in the ASO-II group (in red) with other animal opsins. Only selected regions of the full alignment are shown, with their secondary structure elements displayed at the top. The alignment reveals residues and motifs in the ASO-II group that are broadly conserved throughout the large family of Class A GPCRs, such as the key functional residue D83 (grey) in TM2, a disulphide bridge between C110 in TM3 and C187 in ECL2 (black), and the NPxxY motif in TM7 (blue). Strikingly, ASO-II opsins lack the highly conserved and functionally key E(D)RY motif on TM3 (green). ASO-II opsins also possess residues specific to animal opsins, such as the retinal binding K296 (red). While they do not have E/D at any of the three established counterion positions (yellow), they feature a highly conserved. Glu/Asp at position 292 (orange).

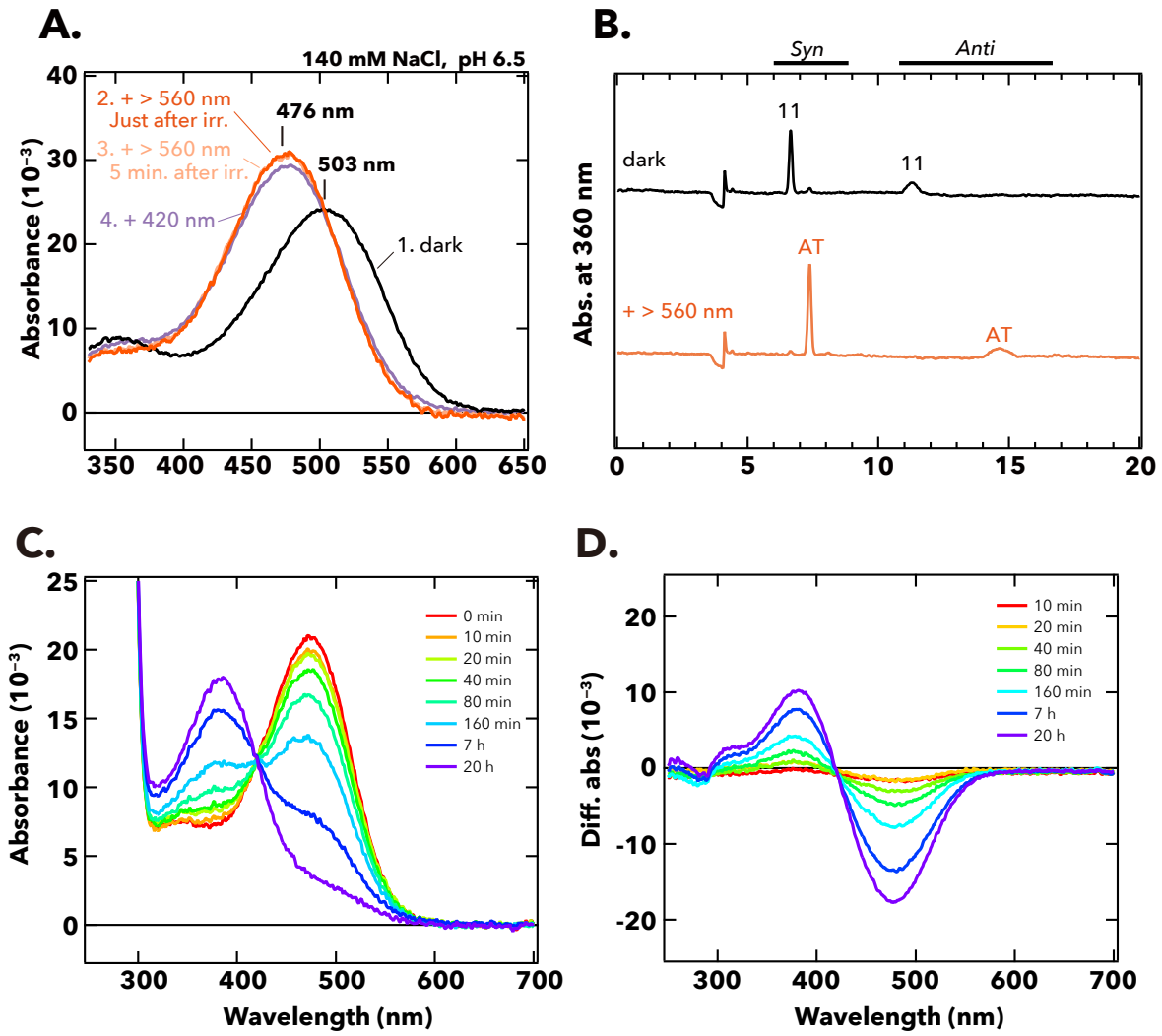

Fig. S3

Fig. S3. Photo- and thermal reactions of wild type Antho2a. (A, B) Absorption spectra and isomer compositions of the chromophore retinal of Antho2a WT before and after light irradiation. (A) Absorption spectra were measured at 0°C in the dark (curve 1, black), after orange light irradiation (> 560 nm, curve 2 and curve 3, deep and pale orange), and after subsequent violet light irradiation (420 nm, curve 4, purple). Irradiation of wild type Antho2a with orange light shifted the absorption maximum from 503 nm in the dark (curve 1, black) to 476 nm in the photoproduct (curve 2 and curve 3, orange). Upon subsequent irradiation with 420 nm light (while the photoproduct was stable), the λ_{max} of the photoproduct stayed at 476 nm, with only a slight decrease of the peak absorbance (curve 4,

purple) possibly resulting from degradation of the photoproducts upon light irradiation. (B) The configuration of retinal in Antho2a WT before (black) and after (orange) irradiation with orange light (> 560 nm) was analysed with HPLC. Retinal was extracted in its oxime form. AT, all-*trans* retinal; 11, 11-*cis* retinal. (C, D) Thermal stability of the photoproducts of wild type Antho2a in 140 mM NaCl at pH 6.5 and 0 °C. (C) Changes in the absorption spectra of Antho2a WT after irradiation with orange (>560 nm) light (with the sample kept in the dark at 0°C). Each coloured curve corresponds to a different time after light irradiation. (D) Difference spectra obtained by subtracting the spectrum of Antho2a WT in the dark from the spectra measured at different time points after irradiation (shown in C).

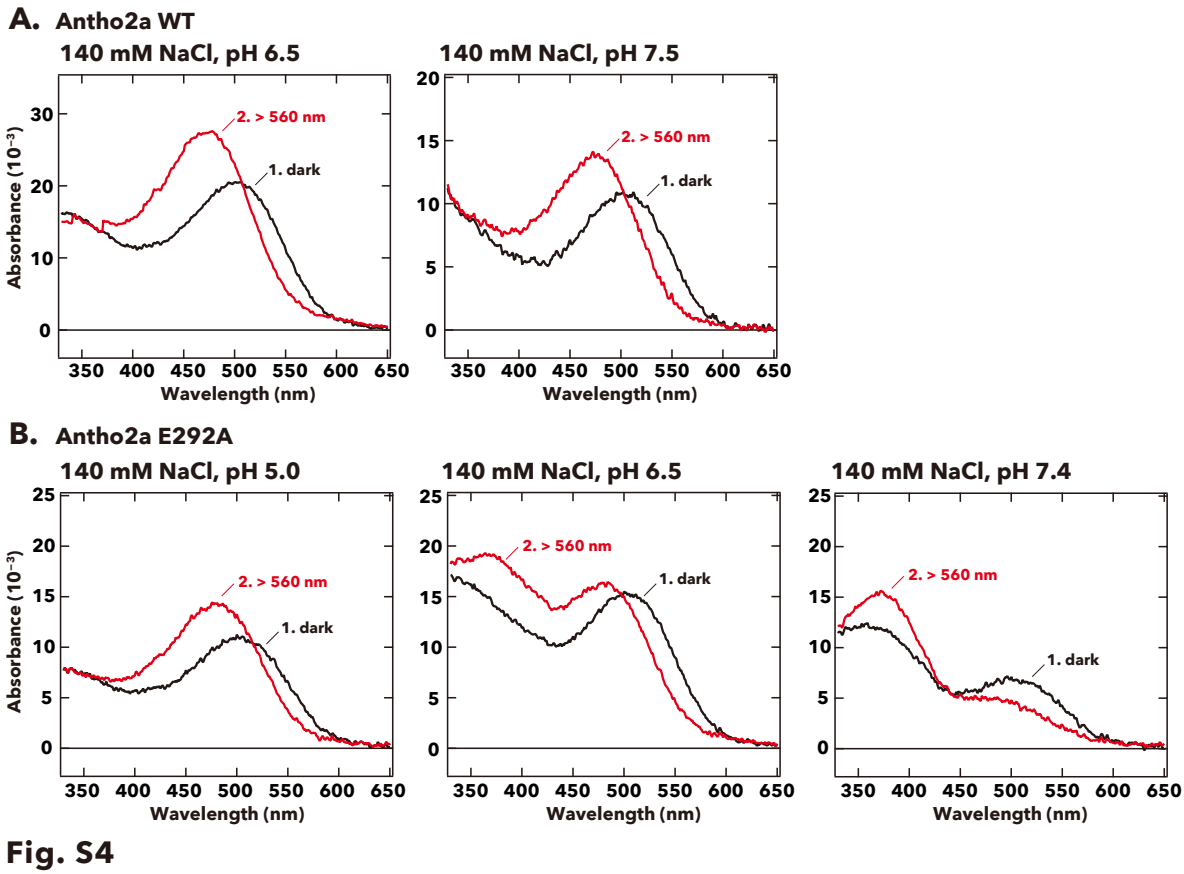

Fig. S4

Fig. S4. (A, B) Effect of pH on the absorption spectra of the dark state and photoproduct of (A) wild type Antho2a and (B) the E292A mutant at 140 mM NaCl. Each graph shows spectra before (curves 1, black) and after (curves 2, red) irradiation with orange (> 560 nm) light.

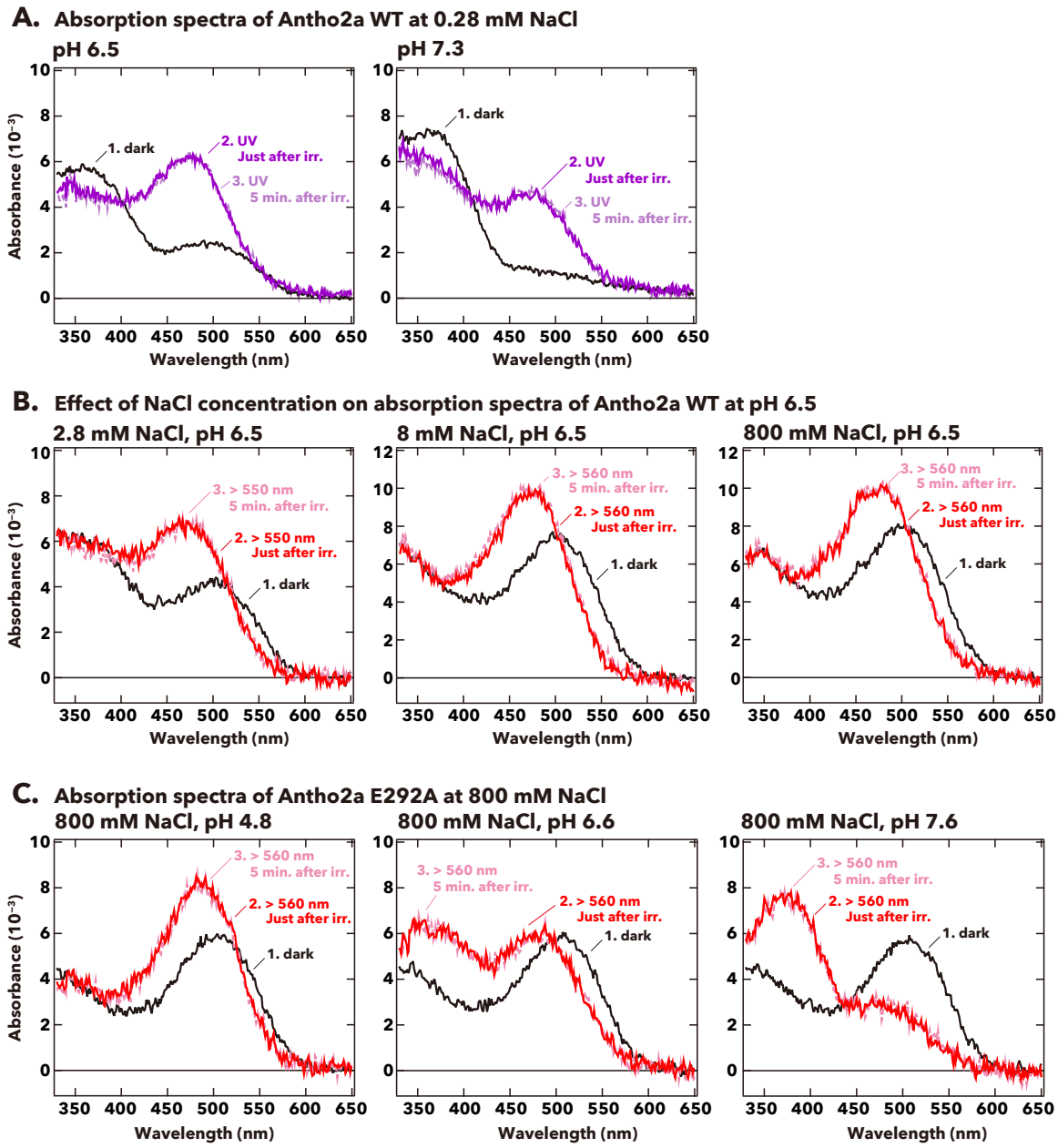

Fig. S5

Fig. S5. Effect of pH and NaCl concentration on absorption spectra of the dark states and photoproducts of Antho2a. (A) Absorption spectra of wild type Antho2a at 0.28 mM NaCl under different pH conditions (pH 6.5 and pH 7.3). (B) Absorption spectra of wild type Antho2a at pH 6.5 with varying NaCl concentrations (2.8 mM, 8 mM, and 800 mM). (C) Absorption spectra of the E292A mutant of Antho2a at 800 mM NaCl and different pH conditions (pH 4.8, pH 6.6, and pH 7.6). Each graph shows spectra before (curves 1, black) and after (curves 2, deep purple/red, and 3, pale

purple/pink) irradiation with UV light (< 410 nm, A) or orange light (> 550 nm or > 560 nm, B and C). Curves 2 and 3 in each graph represent, respectively, the first measurement (immediately after irradiation) and a subsequent measurement (< 5 min. after irradiation). The minimal change in the absorption spectra over this time scale indicates that the spectra remain stable after irradiation.

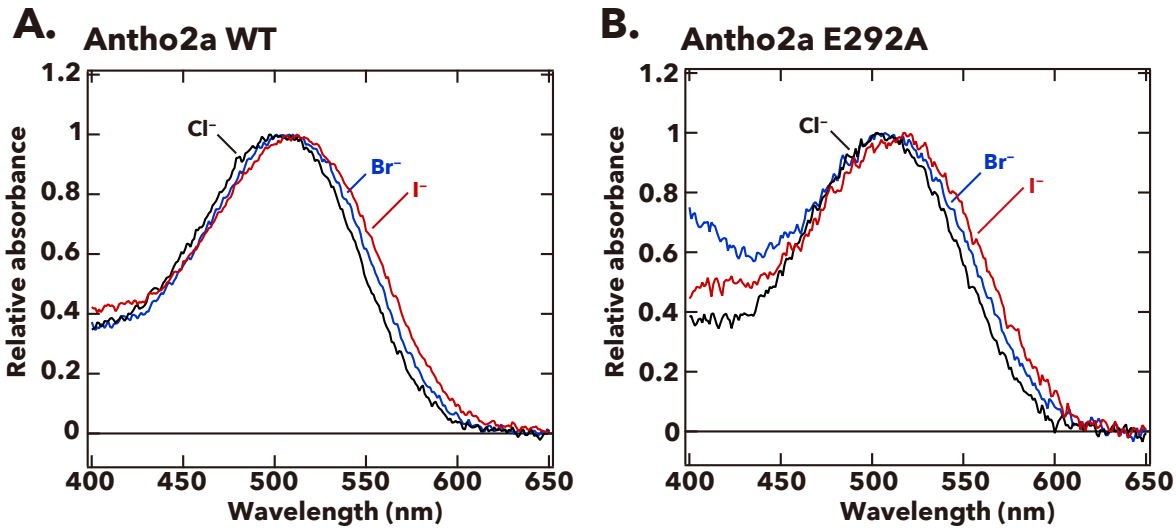

Fig. S6

Fig. S6. Effect of halide anions on the absorption spectra of (A) wild type Antho2a and (B) the Antho2a E292A mutant at pH 6.5 and 0°C. The graphic shows the normalised absorption spectra of the pigments prepared in 140 mM NaCl (black curves), 140 mM NaBr (blue curves), and 140 mM NaI (red curves).

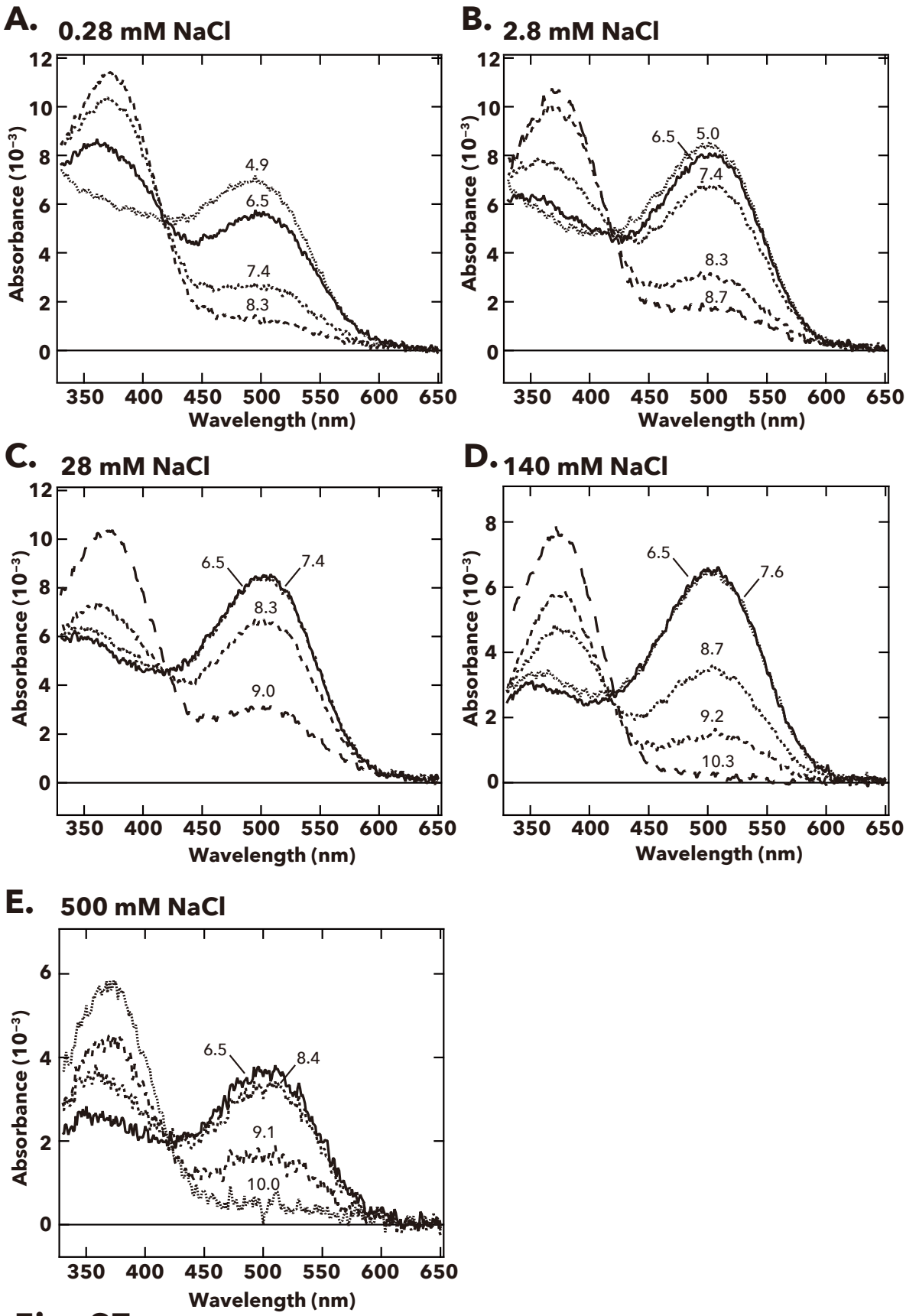
A. 0.28 mM NaCl
B. 2.8 mM NaCl
C. 28 mM NaCl
D. 140 mM NaCl
E. 500 mM NaCl
Absorbance (10⁻³)
Wavelength (nm)
4.9
6.5
7.4
8.3
5.0
8.7
9.0
7.6
9.2
10.3
8.4
9.1
10.0

Fig. S7

Fig. S7. pH-dependent changes in the absorption spectra of Antho2a WT at (A) 0.28 mM, (B) 2.8 mM, (C) 28 mM, (D) 140 mM, and (E) 500 mM Cl^- at 0°C. The pH values of the solution, measured right after each spectroscopic measurement, are indicated on the corresponding curves in each graph.

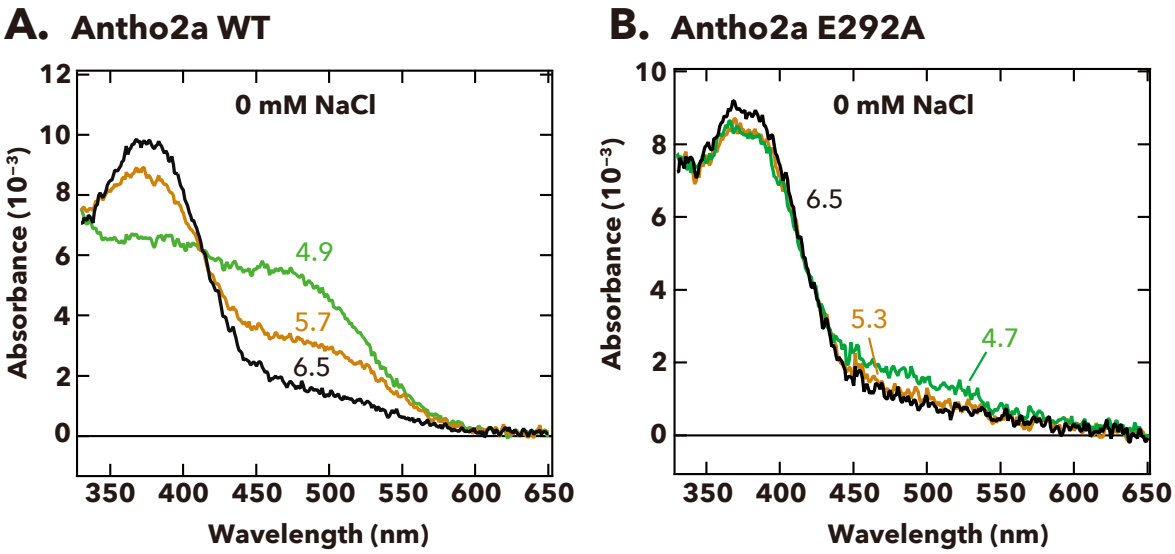

Fig. S8

Fig. S8. pH-dependent changes in the absorption spectra of Antho2a WT and Antho2a E292A at 0 mM NaCl (containing 70 mM Na_2SO_4) at 0°C. The pH values at which the absorption spectra were measured are indicated on the corresponding curves.

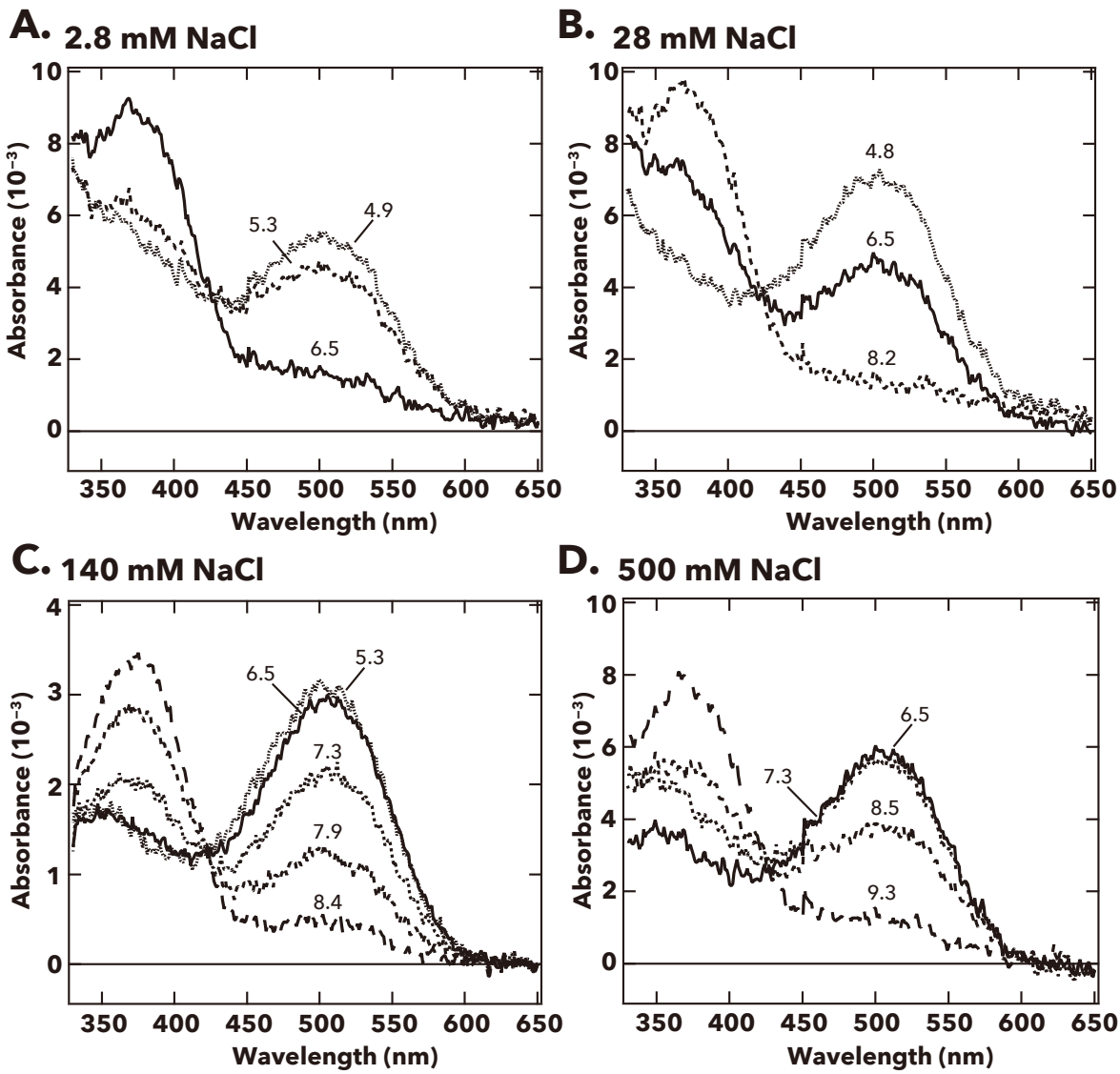

Fig. S9

Fig. S9. pH-dependent changes in the absorption spectra of Antho2a E292A at (A) 2.8 mM, (B) 28 mM, (C) 140 mM, and (D) 500 mM Cl^- at 0°C. The pH values are indicated on the corresponding curves in each graph.

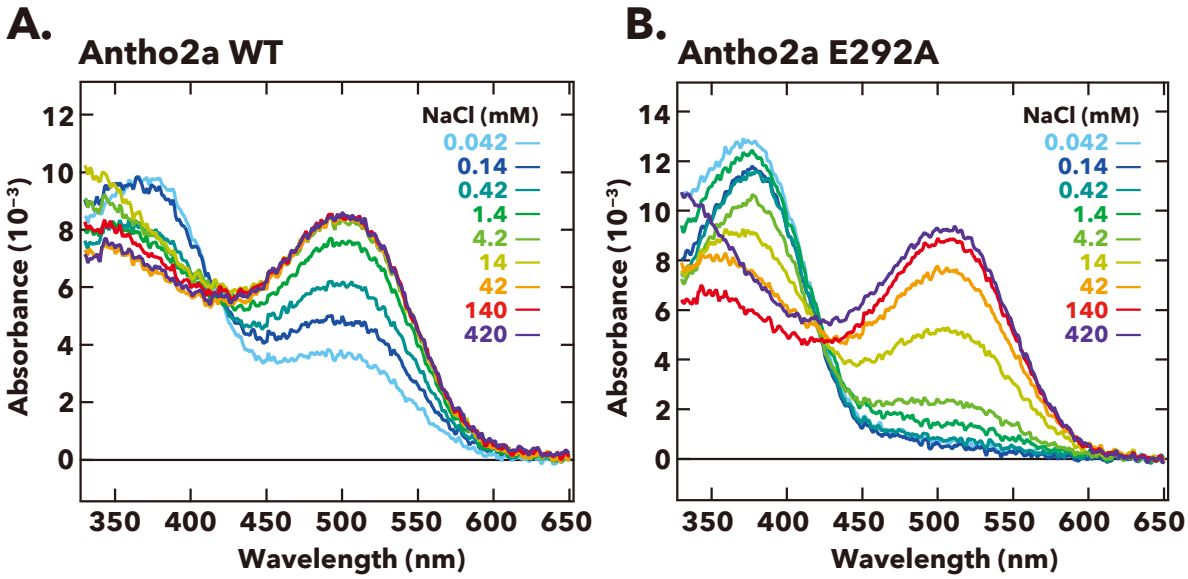

Fig. S10

Fig. S10. Absorption spectra of (A) wild type Antho2a and (B) the Antho2a E292A mutant under different Cl^- concentrations at pH 6.5 and 0°C. Each colour indicates a different concentration of Cl^-.